



Defense Threat Reduction Agency
8725 John J. Kingman Road, MS 6201
Fort Belvoir, VA 22060-6201



DTRA-TR-14-28

TECHNICAL REPORT

Exploration of MEMS G-Switches at 100-10,000 G-Levels with Redundancy

Approved for public release; distribution is unlimited.

April 2014

HDTRA01-11-1-0056

Weinong Wayne Chen

Prepared by:
Purdue University
3323 Neil Armstrong Hall of
Engineering
701 West Stadium Avenue
West Lafayette, IN 47907

DESTRUCTION NOTICE:

Destroy this report when it is no longer needed.
Do not return to sender.

PLEASE NOTIFY THE DEFENSE THREAT REDUCTION
AGENCY, ATTN: DTRIAC/ J9STT, 8725 JOHN J. KINGMAN ROAD,
MS-6201, FT BELVOIR, VA 22060-6201, IF YOUR ADDRESS
IS INCORRECT, IF YOU WISH THAT IT BE DELETED FROM THE
DISTRIBUTION LIST, OR IF THE ADDRESSEE IS NO
LONGER EMPLOYED BY YOUR ORGANIZATION.

REPORT DOCUMENTATION PAGE

Form Approved
OMB No. 0704-0188

Public reporting burden for this collection of information is estimated to average 1 hour per response, including the time for reviewing instructions, searching existing data sources, gathering and maintaining the data needed, and completing and reviewing this collection of information. Send comments regarding this burden estimate or any other aspect of this collection of information, including suggestions for reducing this burden to Department of Defense, Washington Headquarters Services, Directorate for Information Operations and Reports (0704-0188), 1215 Jefferson Davis Highway, Suite 1204, Arlington, VA 22202-4302. Respondents should be aware that notwithstanding any other provision of law, no person shall be subject to any penalty for failing to comply with a collection of information if it does not display a currently valid OMB control number. **PLEASE DO NOT RETURN YOUR FORM TO THE ABOVE ADDRESS.**

1. REPORT DATE (DD-MM-YYYY) 00-04-2014		2. REPORT TYPE Technical		3. DATES COVERED (From - To) 1 Sept. 2011 - 31 Aug. 2012	
4. TITLE AND SUBTITLE Exploration of MEMS G-Switches at 100-10,000 G-Levels with Redundancy				5a. CONTRACT NUMBER HDTRA1-11-1-0056	
				5b. GRANT NUMBER	
				5c. PROGRAM ELEMENT NUMBER	
6. AUTHOR(S) Weinong Wayne Chen				5d. PROJECT NUMBER	
				5e. TASK NUMBER	
				5f. WORK UNIT NUMBER	
7. PERFORMING ORGANIZATION NAME(S) AND ADDRESS(ES) Purdue University 3323 Neil Armstrong Hall of Engineering 701 West Stadium Avenue West Lafayette, IN 47907				8. PERFORMING ORGANIZATION REPORT NUMBER	
9. SPONSORING / MONITORING AGENCY NAME(S) AND ADDRESS(ES) Defense Threat Reduction Agency 8725 John J. Kingman Road STOP 6201 Fort Belvoir, VA 22060 PM/S. Peiris				10. SPONSOR/MONITOR'S ACRONYM(S) DTRA	
				11. SPONSOR/MONITOR'S REPORT NUMBER(S) DTRA-TR-14-28	
12. DISTRIBUTION / AVAILABILITY STATEMENT Approved for public release; distribution is unlimited.					
13. SUPPLEMENTARY NOTES					
14. ABSTRACT The goal of this research program was to develop fundamental understanding necessary for producing novel MEMS/NEMS accelerometers that will characterize acceleration forces in the range of 100-10,000 g with high-precision, high-redundancy, high-frequency-response, high reliability, and high manufacturing repeatability. Such accelerometers consume a small fraction of power as compared to conventional accelerometers, which makes them ideal choices for applications where available power is limited.					
15. SUBJECT TERMS accelerometers MEMS g-switches silicon DRIE					
16. SECURITY CLASSIFICATION OF:			17. LIMITATION OF ABSTRACT UU	18. NUMBER OF PAGES 59	19a. NAME OF RESPONSIBLE PERSON Suhithi Peiris
a. REPORT Unclassified	b. ABSTRACT Unclassified	c. THIS PAGE Unclassified			19b. TELEPHONE NUMBER (include area code) 703-767-4732

CONVERSION TABLE

Conversion Factors for U.S. Customary to metric (SI) units of measurement.

MULTIPLY $\xrightarrow{\hspace{10em}}$ BY $\xrightarrow{\hspace{10em}}$ TO GET
 TO GET $\xleftarrow{\hspace{10em}}$ BY $\xleftarrow{\hspace{10em}}$ DIVIDE

angstrom	1.000 000 x E -10	meters (m)
atmosphere (normal)	1.013 25 x E +2	kilo pascal (kPa)
bar	1.000 000 x E +2	kilo pascal (kPa)
barn	1.000 000 x E -28	meter ² (m ²)
British thermal unit (thermochemical)	1.054 350 x E +3	joule (J)
calorie (thermochemical)	4.184 000	joule (J)
cal (thermochemical/cm ²)	4.184 000 x E -2	mega joule/m ² (MJ/m ²)
curie	3.700 000 x E +1	*giga bacquerel (GBq)
degree (angle)	1.745 329 x E -2	radian (rad)
degree Fahrenheit	$t_k = (t^{\circ}f + 459.67)/1.8$	degree kelvin (K)
electron volt	1.602 19 x E -19	joule (J)
erg	1.000 000 x E -7	joule (J)
erg/second	1.000 000 x E -7	watt (W)
foot	3.048 000 x E -1	meter (m)
foot-pound-force	1.355 818	joule (J)
gallon (U.S. liquid)	3.785 412 x E -3	meter ³ (m ³)
inch	2.540 000 x E -2	meter (m)
jerk	1.000 000 x E +9	joule (J)
joule/kilogram (J/kg) radiation dose absorbed	1.000 000	Gray (Gy)
kilotons	4.183	terajoules
kip (1000 lbf)	4.448 222 x E +3	newton (N)
kip/inch ² (ksi)	6.894 757 x E +3	kilo pascal (kPa)
ktap	1.000 000 x E +2	newton-second/m ² (N-s/m ²)
micron	1.000 000 x E -6	meter (m)
mil	2.540 000 x E -5	meter (m)
mile (international)	1.609 344 x E +3	meter (m)
ounce	2.834 952 x E -2	kilogram (kg)
pound-force (lbs avoirdupois)	4.448 222	newton (N)
pound-force inch	1.129 848 x E -1	newton-meter (N-m)
pound-force/inch	1.751 268 x E +2	newton/meter (N/m)
pound-force/foot ²	4.788 026 x E -2	kilo pascal (kPa)
pound-force/inch ² (psi)	6.894 757	kilo pascal (kPa)
pound-mass (lbm avoirdupois)	4.535 924 x E -1	kilogram (kg)
pound-mass-foot ² (moment of inertia)	4.214 011 x E -2	kilogram-meter ² (kg-m ²)
pound-mass/foot ³	1.601 846 x E +1	kilogram-meter ³ (kg/m ³)
rad (radiation dose absorbed)	1.000 000 x E -2	**Gray (Gy)
roentgen	2.579 760 x E -4	coulomb/kilogram (C/kg)
shake	1.000 000 x E -8	second (s)
slug	1.459 390 x E +1	kilogram (kg)
torr (mm Hg, 0 ^o C)	1.333 22 x E -1	kilo pascal (kPa)

*The bacquerel (Bq) is the SI unit of radioactivity; 1 Bq = 1 event/s.

**The Gray (GY) is the SI unit of absorbed radiation.

Executive Summary

Exploration of MEMS G-Switches at 100-10,000 G-Levels with Redundancy

DTRA Grant: HDTRA1-11-1-0056

Period of Performance: 01 September 2011 through 31 August 2012

PI: Weinong Wayne Chen, Purdue University

Co-PIs: Dimitrios Peroulis and Alina Alexeenko, Purdue University

The goal of this research program is to develop fundamental understandings necessary for producing novel MEMS/NEMS accelerometers that will characterize acceleration forces in the range of 100-10,000 g with high-precision, high-redundancy, high-frequency-response, high reliability, and high manufacturing repeatability. Such accelerometers consume a small fraction of power as compared to conventional accelerometers, which makes them ideal choices for applications where available power is limited.

A novel MEMS g-switch has been designed, fabricated, packaged, and tested. In accordance with simulations and beam dynamics design metrics for survivability to high-g acceleration levels, three different configurations of possible 100-g switches were designed. The devices were fabricated on low resistivity ($<0.01 \Omega\text{-cm}$) silicon on insulator wafers (SOI) using standard micromachining techniques. Fixed-fixed beams created from SOI wafers have uniform single-crystal nature, negligible and repeatable residual stress. The Fixed-fixed beams have widths in the order of 6-10 μm and thickness of 100 μm for a deflection of 5 μm corresponding to different acceleration level of 100 g. The beams are fabricated in a 0.3 cm by 0.3 cm die which is then packaged and wire bonded in a ceramic package, which is then placed in a tungsten carbide package and potted with STYCAST 1090SI for shock testing and evaluation. The results of low g experiment have shown that the fabricated devices trigger in the ranges of 64 – 157 g and shock experiments show that the devices survive acceleration impacts in the range of 29,000 g. These were found to be in close correspondence with the dynamic simulations for the fabricated device with the same acceleration profile. Analysis is being conducted on the failure of the silicon beams as the size decreases and loading rate increases and ability to increase survivability under high-g loads.

Due to the feasibility demonstrated in this research program, the novel accelerometers developed have strong potentials to be adapted in applications in the near future. This report summarizes the technical achievements realized during the performance period of this research program.

Table of Contents

Executive Summary	i
1. Introduction.....	1
1.1 Background	1
2. Technical Approach	2
2.1 Development of MEMS Accelerometer.....	2
2.1.1 System Overview	2
2.1.2 Silicon as a Fabrication Material	3
2.1.3 MEMS Design Fundamentals	5
2.1.4 Device Sizing Methodology and Dimensions.....	6
2.1.5 Dynamic Effects.....	9
2.1.6 Fabrication Process Flow	15
2.2 Experimental Evaluation	17
2.2.1 Packaging Process.....	17
2.2.2 Electrical Setup	17
2.2.3 Experimental Results:	19
2.3 Simulation Comparison.....	23
2.4 Failure analysis.....	28
2.5 Acceleration Evaluation setup:.....	29
2.5.1 Low-g measurement Setup:	30
2.5.2 High-g measurement Setup:.....	31
2.5.3 Experimental Procedure:.....	33
2.5.4 Potential sources of Experimental Error:	33
2.5.5 Data Processing:.....	34
2.6 Concluding Remarks	37
2.7 Possible Future Directions	37
3. References.....	41
4. Appendix A.....	43
.....	43

1. Introduction

1.1 *Background*

Measurements of rapidly varying acceleration/deceleration environments, such as those encountered by a penetrator moving through a complex target are critical for weapon system applications and are required with high fidelity and reliability. An acceptable acceleration sensor must be capable of surviving extreme acceleration conditions up to 100,000 g's, yet functioning accurately in lower shock environments of 100 to 10,000 g's. Traditionally, a mass-spring type of accelerometer is used to detect acceleration-time histories. When the acceleration history varies rapidly, the inertia-based sensor becomes less accurate but highly noisy. Furthermore, it is difficult to achieve redundancy in measurements as each of the mass-spring system behaves differently and susceptible to failures. The high power consumption of these accelerometers also challenges the on-board power-supply system and makes redundancy even less possible. Innovative approaches are necessary to obtain accurate and reliable measurements of such fluctuating environments.

In present technology, there are a number of commercial accelerometers that have been developed and employed in real systems. The most commercially used piezoelectric accelerometer of this type is the Endevco 7270 series which can be used to measure acceleration histories up to 200,000 g. However, a history of failure under lower-g shock loads has been seen in such accelerometer. For instance, 200,000-g accelerometers have failed under 10,000-g shock loads. Analysis on the failure modes of this accelerometer can be found in [1]. In about half of the devices that failed, failure was due to the damage to the proof mass. Given that no redundancy exists, failure in the proof mass leads to a total failure in the accelerometer.

Another commercial accelerometer is the Silicon design 1220, which is similar in design to the SDI 1210. Sensing in this accelerometer is of the capacitive type with a max detection of 6,000 g. These were found to suffer from a time shift in the output and fail under shock loads of about 70,000 g due to damage to the sensing electrodes and proof mass [2].

The Analog Devices ADX 181-100 is another state-of-the-art capacitive accelerometer, which measures acceleration level up to 1,000 g via capacitive sensing. Sensing in this accelerometer is done via 40 individual sensing cells with each cell measuring acceleration independently, thus offering redundancy to the device. However the acceleration pulse width detected by this accelerometer was found to be less than the actual applied profile. In addition, there was a lag in detection (up to 260 μ s) when subjected to shock loads of 60,000 g [2] and are subject to mounting failures.

In order to overcome these limitations, we propose a system consisting of an array of single-crystal silicon (SCS) micro-beams that respond to different acceleration levels by having

multiple beams making solid-to-solid contacts for a given acceleration level. This method has been shown to offer high redundancy and ensures an adequate confidence level in the measure data as shown in the high-g project (HDTRA1-08-1-0026). This is critical when this sensor is used to trigger events with potential severe consequences.

The small sizes and low power consumption also make redundant measurements possible. Variations in the switching mechanism dimensions can tune the switch to close at a very specific range of acceleration. This concept can be expanded to 3-D applications with minimal changes in design. Furthermore, we explore the analytical and numerical modeling of these devices and evaluate their performance under controlled laboratory experimental capabilities.

2. Technical Approach

2.1 Development of MEMS Accelerometer

2.1.1 System Overview

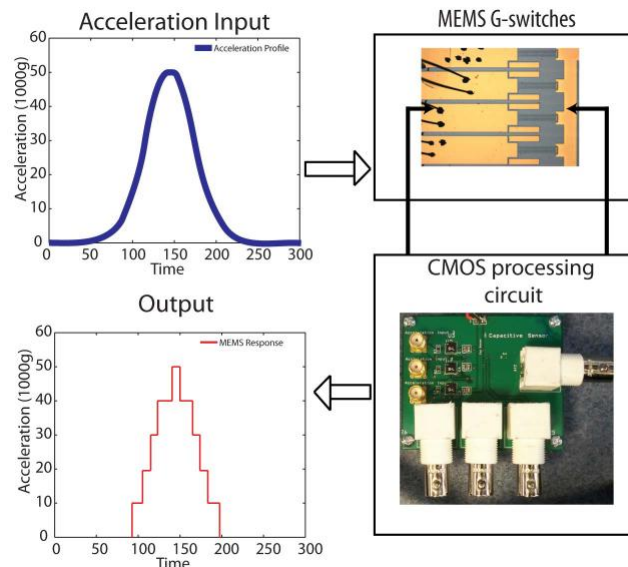


Figure 1: Overview of the proposed accelerometer design.

The design concept for the proposed accelerometer that can be created using cantilevers is shown in Figure 1. In this design concept, a number of single-crystal silicon MEMS g-switches are connected in parallel with the measuring circuit shown. This leads to a “piano approach” in acceleration detection with each set of beams responding to a designed acceleration level. The needed number of beams for each acceleration level depends on the desired confidence level needed for the measurement. When the system is subjected to the acceleration profile shown in Figure 1, a CMOS circuit first reads the raw response. The response would then be processed with this circuit acting as a digital filter in order to filter the noise spikes and contact bouncing due to impact vibrations.

Previous research has provided some insight on the impact phenomena on typical MEMS DC switches, particularly on their failure such under such impact load conditions [5], [6]. Behavior of silicon-to-silicon contact cantilevers also been completed. In order to effectively design the accelerometer for high-g loads, we need to gain a fundamental understanding of the behavior of silicon MEMS cantilevers under high-g loading. This includes the following main characteristics

- 1) Silicon as a fabrication material & g-switch analytical design metrics
- 2) Dynamic simulation on MEMS structures
- 3) Evaluation of g-switches under low and high-g conditions.

2.1.2 Silicon as a Fabrication Material

In order to design and fabricate an effective MEMS accelerometer we needed to choose a suitable fabrication material. Single-crystal silicon is ideal for micromechanical moving structures due to its a) nearly defect-free nature, b) immunity to process-induced material-property variations (properties of silicon wafers are extremely well controlled), c) creep-free structure, and d) the wide manufacturing basis of silicon electronics. For instance, research shown at [7] has shown silicon to be creep free as indicated in Figure 2.

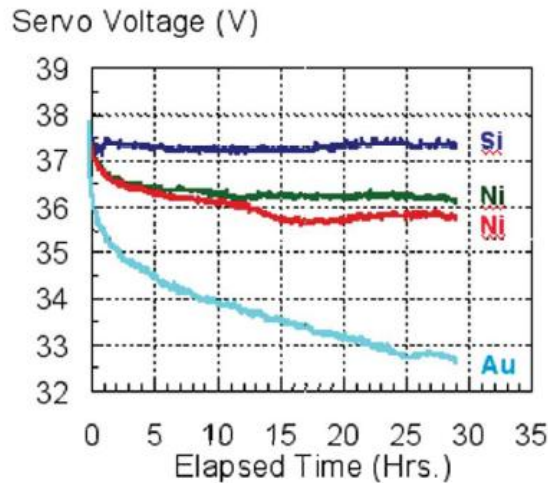


Figure 2: Long term needed bias to maintain a constant deflection for different cantilever materials in air [7].

Since the proposed MEMS device works by sensing a close or open contact, a suitable contact material need to be decided for ideal operation under high-g loads. The contact material for such conditions should exhibit low adhesion forces, high resistance to impact damage, and potential for repeatable low-cost fabrication particularly in a CMOS foundry. Silicon satisfies these requirements and was also chosen as a contact material as well. In addition, the formation of native oxide on this material during operation gives it the potential for self-healing.

Silicon-to-silicon contacts have not been adequately characterized in the literature. As a result, we investigated its suitability for this application during the High-G project. Test structures (Figure 3) were fabricated on Silicon-on-Insulator (SOI) wafer with a device and handle layer resistivity of $0.01 \Omega\text{-cm}$ and device layer thickness of $2 \mu\text{m}$.

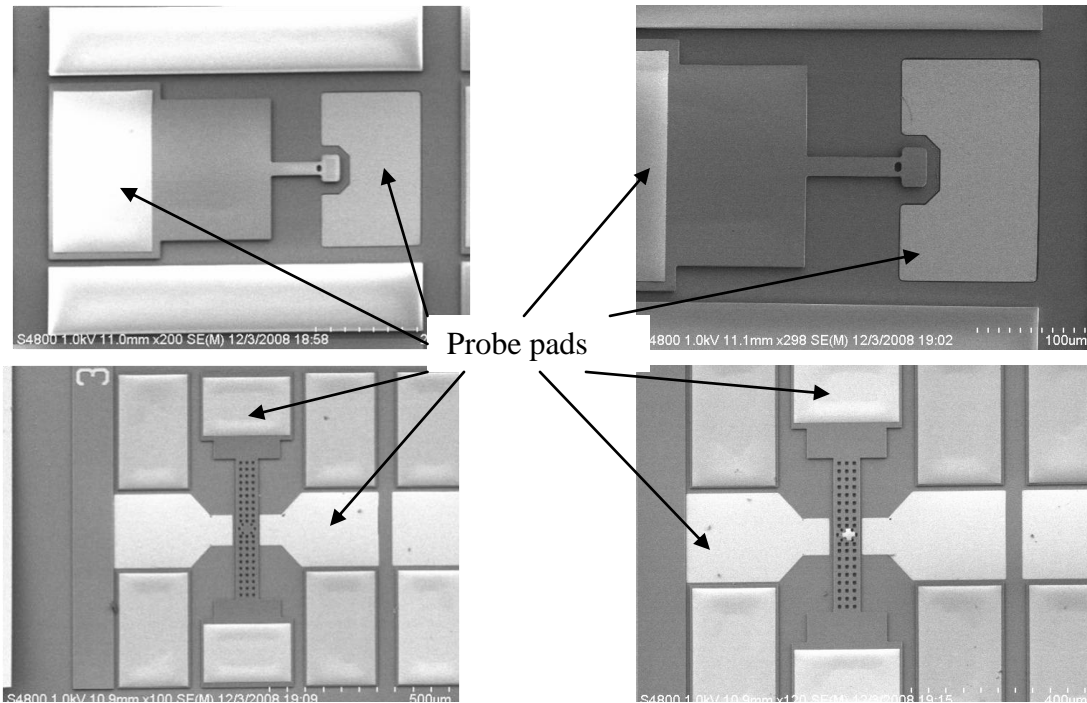


Figure 3: Fabricated silicon test structures. These structures were utilized to evaluate the contact resistance

These devices were electrostatically actuated and were found to have actuation voltages between 20-30 V and contact resistances in the order of 3-4 $k\Omega$ (Figure 4). These devices were also tested with an automated force measurement setup. These results show that silicon to silicon contacts but are well-suited for measuring contact based events such as the one proposed in this project. Although repeatability was not formally characterized, no degradation was observed in our laboratory after many 100s of cycles even in an open unpackaged environment.

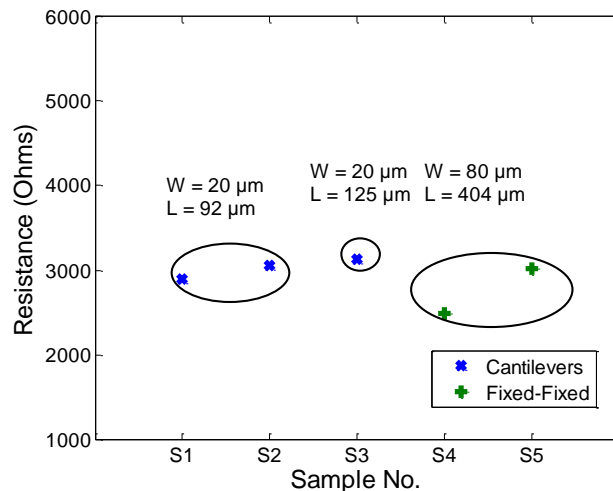


Figure 4: Contact resistance of the silicon test structures

2.1.3 MEMS Design Fundamentals

The g-switch system consists of three main components. First, there is a large mass designed to respond to the intended acceleration levels. Second, a structure of support beams is placed to support the mass and provide stiffness to resist motion. Last, system of sensors is included to detect the motion of the mass and provide additional stiffness and stress relief after the block has moved beyond a specified threshold. An overview of the design is shown in Figure 5

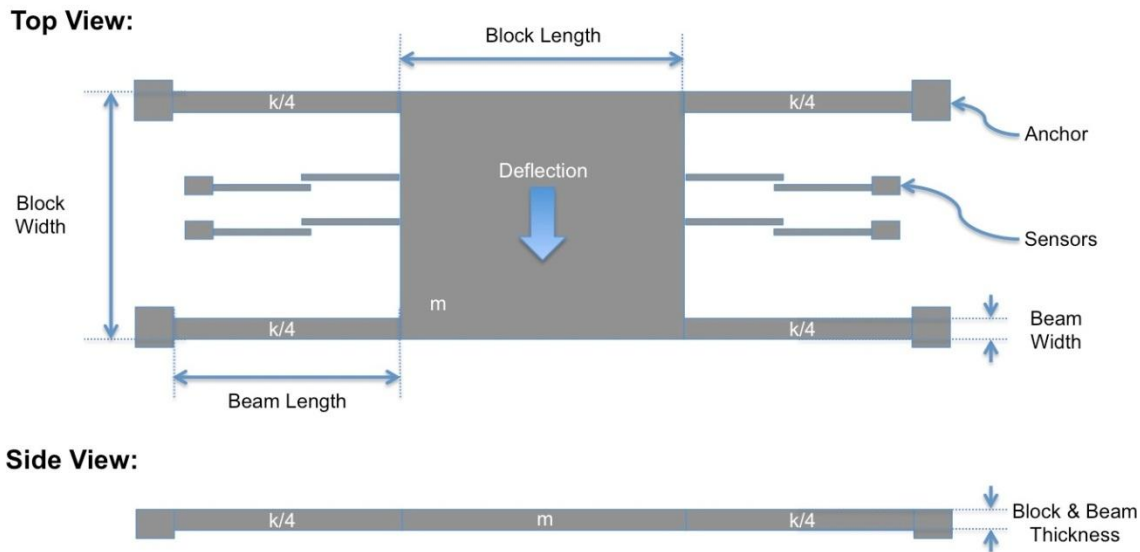


Figure 5: Schematic of device design

The requirement of the sensitivity to low acceleration levels (on the order of 100 g) while surviving extremely high acceleration levels (on the order of 100,000 g) necessitates the use of mass sufficiently large relative to the surrounding structure. This prompted a design that essentially decouples the mass size from the stiffness.

As shown in Figure 5, a relatively large, rectangular block was chosen for the proof mass. The block is supported by four rectangular beams, which behaves with fixed-fixed boundary conditions during motion. The entire system is suspended above the main surface of the substrate, and the far ends of the support beams are anchored to the surface. Additionally, a system of smaller cantilever beams forms the sensing mechanism.

When the system is exposed to an acceleration acting in the vertical direction, the block will move and the support beams will act as a spring, resisting the motion. After a specified displacement, the sensor beams will contact. Any displacement beyond this point will experience increased effective spring stiffness, due to the sensors. Using this staggered stiffness design, a device can be created that will respond to lower acceleration levels yet survive higher loads.

2.1.4 Device Sizing Methodology and Dimensions

Several factors were taken into account when determining the device dimensions, which are listed below:

1. Fabrication methods limit the minimum width and thickness of components as well as constraining the maximum depth of the overall system.
2. Both the peak static and dynamic stresses must be below the maximum allowable threshold for the material.
3. Additionally, to cause a readable resistance drop to measure contact, a minimum force requirement must be met. A force threshold must be surpassed to cause consistent release from contact.

Considering the above factors, the following method was used to size the central block, which plays a dominant role in determining the system size.

Assuming steady state:

$$F_a = F_{s,sen} + F_{s,sup} \quad (1)$$

Where:

F_a = force due to acceleration

$F_{s,sen}$ = total force due to the sensor beams

$F_{s,sup}$ = total force due to the support beams

Substituting in expressions for each force into Equation 1 yields:

$$\rho V_b a_m = k_{sup} x + k_{sen} (x - g) \quad (2)$$

Where:

a_m = peak acceleration for design to measure

ρ = material density (silicon)

V_b = block volume

k = effective spring stiffness

x = displacement from relaxed position

g = initial sensor gap before contact

The following expressions were used to set minimum contact and restoring forces:

$$F_{res} = k_{sup} g \quad (3)$$

$$F_{con} = F_{s,sen} = k_{sen} (x - g) \quad (4)$$

Where:

F_{res} = restoring force

F_{con} = contact force

The support force can now be rewritten:

$$F_{s,sup} = k_{sup}x = k_{sup}(x - g) + k_{sup}g \quad (5)$$

$$F_{s,sup} = \frac{k_{sup}}{k_{sen}}F_{con} + F_{res} \quad (6)$$

Substitution into the original force equation (Equation 1) yields the minimum block volume:

$$V_b \geq \left(\frac{k_{sup}}{k_{sen}} + 1 \right) \frac{F_{con}}{ra_m} + \frac{(F_{res})_{min}}{ra_m} \quad (7)$$

As stated in Equation 7, the minimum block volume is dependent on the ratio of total stiffness values. It is desirable to make this ratio as small as possible, and a constraint can be imposed on this ratio using the intended peak acceleration for survival. Assuming a specified deflection when experiencing the peak survivable load, the force balance given in Equation 1 will yield the following:

$$rV_b a_s = k_{sup}(g + d) + k_{sen}d \quad (8)$$

Where:

a_s = maximum survivable load

d = maximum deflection beyond contact

Converting this expression to be in terms of the original acceleration force yields:

$$rV_b a_m = k_{sen} \left(\frac{k_{sup}}{k_{sen}}(g + d) + d \right) \frac{a_m}{a_s} \quad (9)$$

Equating the right hand side of Equation 2 and 9, and solving for the stiffness ratio yields:

$$\frac{k_{sup}}{k_{sen}} = \sqrt{\frac{F_{res} \left[\frac{a_s}{a_m} - \left(\frac{d}{g} + 1 \right) \right]^{-1} \frac{d}{g} + \frac{1}{4} \left\{ 1 + \frac{F_{res}}{F_{con}} + \left[\frac{a_s}{a_m} - \left(\frac{d}{g} + 1 \right) \right]^{-1} \right\}^2}{-\frac{1}{2} \left\{ 1 + \frac{F_{res}}{F_{con}} + \left[\frac{a_s}{a_m} - \left(\frac{d}{g} + 1 \right) \right]^{-1} \right\}}} \quad (10)$$

This expression can now be used in Equation 7 to size the block. Assuming a maximum allowable value of 0.008 for strain, the support and sensor beams can now be sized. Bending strain is directly proportional to the second derivative of deflection. The support beams act as a fixed-fixed cantilever beam; therefore both the first and second derivatives of the deflection will be zero at each end. Using these boundary conditions, the expression for maximum strain due to static deflection is the following:

$$e_{max} = \frac{w_s}{2} y_{max}'' = \frac{w_{sup} L_{sup} (F_{s,sup})_{max}}{4EI_s n_{sup}} \quad (11)$$

Where:

- L_{sup} = support beam length
- w_{sup} = support beam width (viewed from above)
- I_{sup} = support beam bending moment
- E = material Young's modulus
- y = beam deflection
- n = number of support beams
- ε = bending strain

The relation between support stiffness and deflection states:

$$\frac{(F_{s, sup})_{max}}{n_{sup}} = \frac{k_{sup} x_{max}}{n_{sup}} = \frac{k_{sup} (g + d)}{n_{sup}} \quad (12)$$

The expression for stiffness of a fixed-fixed beam:

$$\frac{k_{sup}}{n_{sup}} = \frac{12EI_{sup}}{L_{sup}^3} \quad (13)$$

Substitution of Equations 12 and 13 into Equation 11 yields:

$$e_{max} = \frac{w_{sup}}{2} y_{max}^{\circ} = \frac{3w_{sup} (g + d)}{L_{sup}^2} \leq 0.008$$

This criterion is used as a limitation for support width and length values. The support beams are sized using a specified initial sensor gap, and consequently a specified stiffness:

$$\frac{k_{sup}}{n_{sup}} = \frac{(F_{s, sup})_{contact}}{n_{sup} g} = \frac{(rV_b a_m - F_{con})}{n_{sup} g} \quad (14)$$

Substitution of Eq. 13 into the above expression yields the following ratio:

$$\frac{w_{sup}}{L_{sup}} = \sqrt[3]{\frac{(rV_b a_m - F_{con})}{n_{sup} g E t_{sup}}} \quad (15)$$

Where:

- t_{sup} = support beam thickness

From the relationship given in Equation 15, it is seen that for a given set of conditions, the ratio of width to length of the support beams is now a fixed value. To minimize the size of the overall system, it is desirable to have the shortest possible support beam length. Therefore, the smallest feasible width should be used. By fixing this dimension, the length is then established using this ratio.

Due to the use of an SOI wafer, the support beam thickness is fixed and is equal to the thickness of the block and the overall system. With the thickness of the block chosen, the width and length of the block can now be determined so that the block volume meets the requirement listed in Equation 7. To minimize the system size the smallest possible block was chosen, and the aspect ratio of the block width to length was left at unity for the sake of simplicity.

Since all of the dimensions for the block and support beams are determined, the sensor beams can now be dimensionalised. The stiffness ratio was found using Equation 10, so the total sensor system stiffness can be found using the support stiffness from Equation 14. The sensors consist of several pairs of overlapping cantilever beams, for which it can be assumed that they behave effectively similar to fixed-fixed beams with a length equal to the sum of the individual beams minus the overlap distance at the point of contact. The bending moment will be the same as for the cantilevers. Therefore, stresses and dimensions can be calculated for the sensors in a manner similar to the support beams, as follows.

Using a relation similar to Equation 13, the dimensions of the sensors can be found.

$$\frac{k_{sen}}{n_{sen}} = \frac{12EI_{sen}}{L_{sen}^3} \quad (16)$$

Solving this expression for the ratio of width to length yields:

$$\frac{w_{sen}}{L_{sen}} = \sqrt[3]{\frac{k_{sen}}{n_{sen}t_{sen}E}} \quad (17)$$

Using a specified minimum designable width and a chosen overlap region of 5 μm , all of the sensor dimensions can now be found in a manner similar to the support beams. A summary of sample device dimensions for systems designed to switch at 100 g and 150 g of acceleration are listed in Table 1.

Design No.	Load (g)	System Thickness (μm)	Block Width (μm)	Support Width (μm)	Support Length (μm)	Sensor Width (μm)	Sensor Length (μm)	Initial Gap (μm)
1	100	100.0	810.6	6.00	822.60	30	290.5	5.00
2	100	100.0	810.6	8.00	1096.7	30	290.5	5.00
3	100	100.0	810.6	10.0	1370.9	30	290.5	5.00
4	150	100.0	661.99	8.00	1096.49	30	331.98	5.00

Table 1: Designed dimensions for several test case systems

2.1.5 Dynamic Effects

This section deals with the dynamic effects in the beams with emphasis particularly on how the dynamic response affects the maximum stress in the beam. The 1-D model based on Euler-Bernoulli beam theory that was described earlier was used in this analysis. Though the

accelerometer design considered in this work has four beams attached to the block mass that responds to low acceleration levels, only one of the beams is analyzed to quantify the dynamic effects on stress. As a result, the following assumptions are used in the analysis. The beam is analyzed as a guided end cantilever beam with a tip load that is equivalent to $1/4^{\text{th}}$ the force on the block due to external acceleration. It is also assumed that the fluid damping plays a role only at the block location since the gap size between the beam and the substrate is much larger. A bell-shaped acceleration profile as shown in Figure 6 is used for all simulations. The maximum value of the acceleration is varied from 1000 g to 10E6 g to understand the influence of the peak acceleration on dynamic effects.

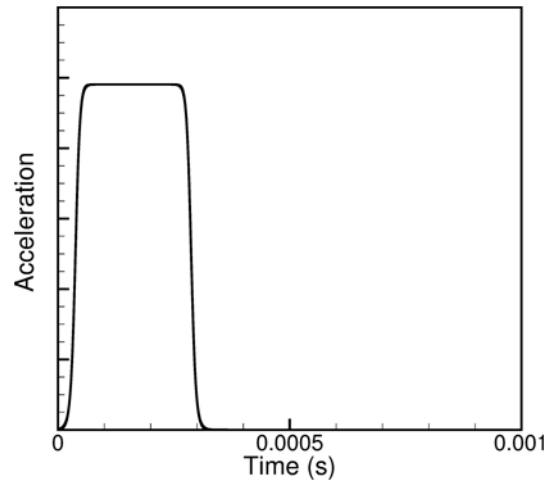


Figure 6: A typical acceleration profile used for the dynamic stress analysis simulations

One important dynamic effect in MEMS switches is the stress wave that is generated due to the contact and then travels through the beam. This stress wave is reflected at the fixed end and can travel back and forth. The influence of the stress wave increases with the impact velocity during contact which in turn depends on the peak acceleration and the geometrical parameters of the beam. Figure 7 shows the time variation of the displacement of the guided end and the absolute maximum of the stress at any location in the beam.

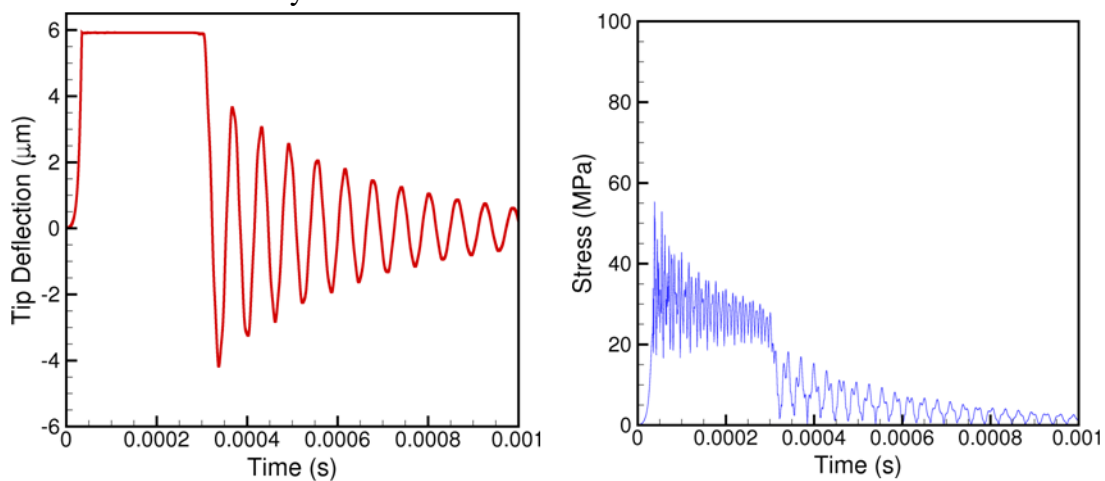


Figure 7: Time dependence of the tip displacement and the absolute maximum of the bending stress in the beam for a peak acceleration of 1000 G.

It can be clearly seen that the block makes contact with the substrate and remains in contact till about 300 μs . Once the external acceleration is removed, the beam oscillates about its initial position before coming to rest gradually. It can also be seen in Figure 7 that the absolute maximum of the bending stress over the entire duration is about 55 MPa which is higher than just the static bending stress. However, the stress is still much lower than the yield stress thereby predicting that the beam under consideration will not fail for a peak acceleration of 1000 g.

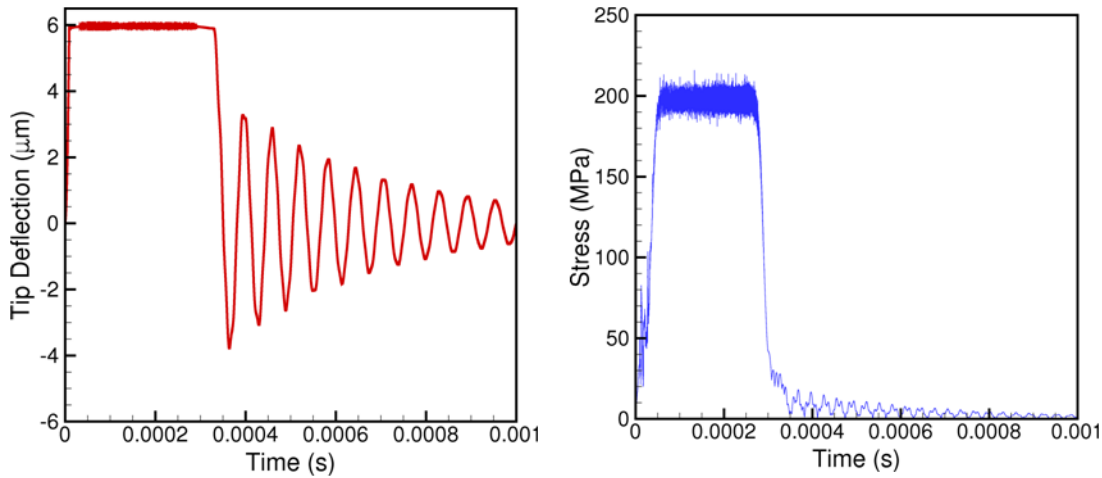


Figure 8: Time dependence of the tip displacement and the absolute maximum of the bending stress in the beam for a peak acceleration of $100e3$ g.

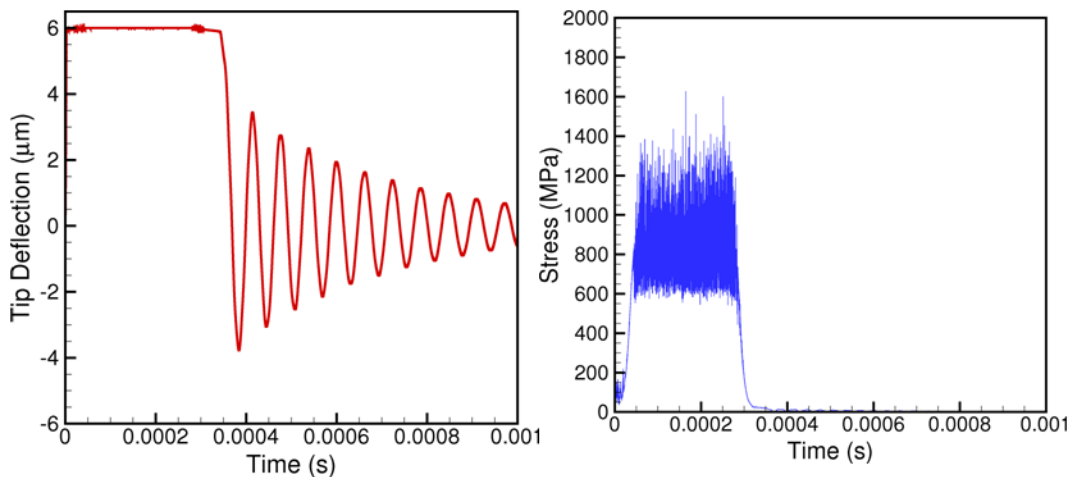


Figure 9: Time dependence of the tip displacement and the absolute maximum of the bending stress in the beam for a peak acceleration of $1e6$ g.

Similar analyses for a peak acceleration of $100e3$ g and $1e6$ g were performed with results shown in Figures 8 and 9. Though the displacement profiles do not change significantly, the value of the absolute maximum of the bending stress increases rapidly with the maximum bending stress reaching a value of about 1.6 GPa for a peak acceleration of $1e6$ g indicating that the beam is likely to fail. The one-dimensional model clearly captures the dynamic effects and also the traveling stress wave which results in the oscillation of bending stress at any given location in the

beam. Figures 10(a) to (d) show travelling stress wave for the beam in Figure 9 at from time $t = 2.26 \mu\text{s}$ to $14 \mu\text{s}$ for the applied load of 1MG as the beam comes into contact. Figures 10 (e) & (f) shows the stress waves when beam breaks contact.

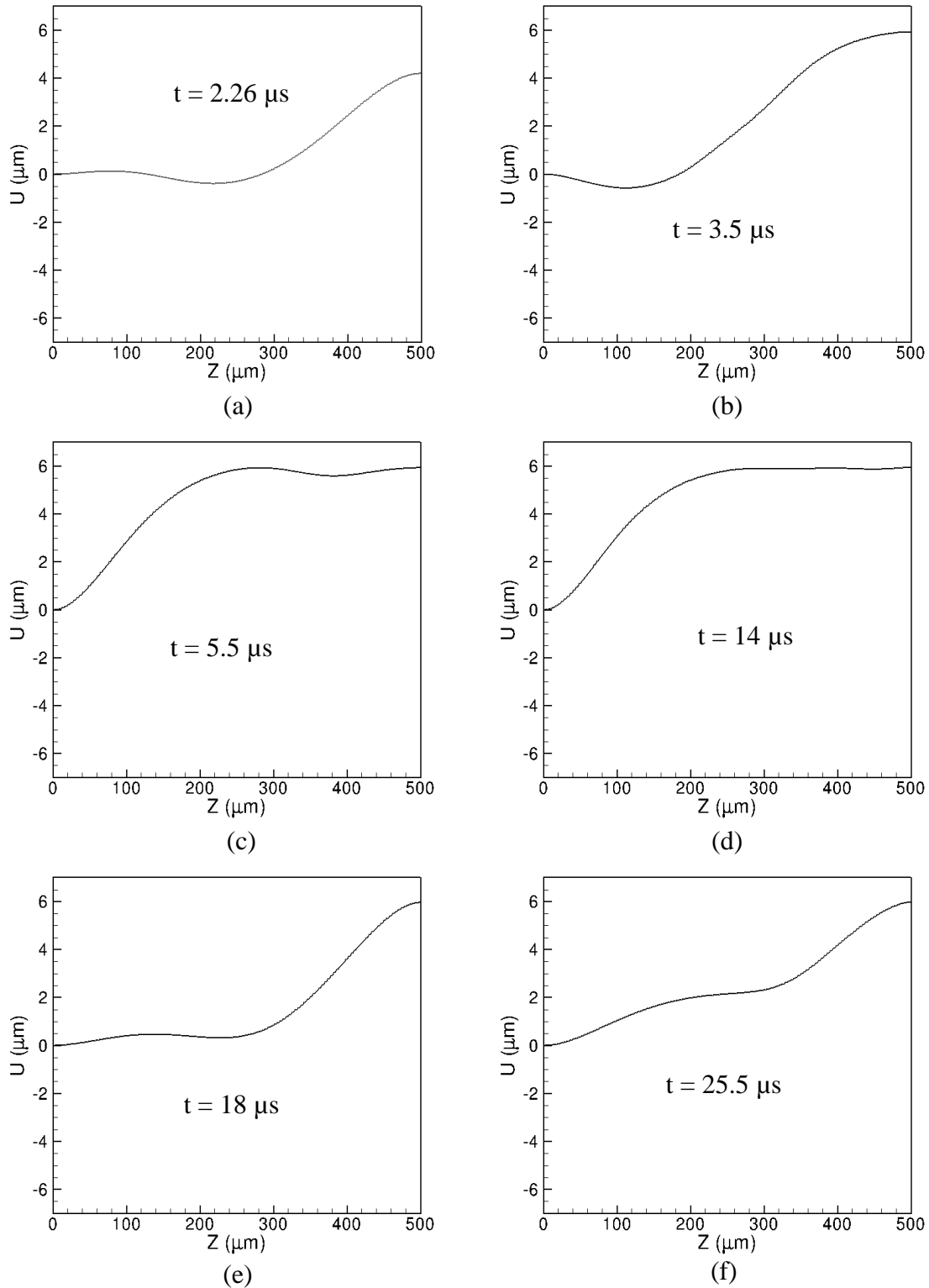


Figure 10: Time dependence of the beam profile of the beam in Figure 9 for a peak acceleration of $1e6 g$.

It should also be mentioned that the maximum stress does not always occur at the fixed end indicating that the stress wave travels back and forth along the length of the beam.

In order to evaluate the dependence of various beam parameters on the maximum bending stress, the analysis was repeated for three different designs with dimensions summarized below. It should be mentioned that the geometrical parameters are very similar to the dimensions of the final design of Table 1

	Block dimensions (L(μm) x b(μm) x h(μm))	Beam dimensions (L(μm) x b(μm) x h(μm))	Theoretical response acceleration (g)
Design 1	704.3 x 704.3 x 100	1032.5 x 8 x 100	150
Design 2	862.6 x 862.6 x 100	1032.5 x 8 x 100	100
Design 3	704.3 x 704.3 x 100	774.6 x 6 x 100	150

Table 2: Beam dimensions used in dynamic simulations

It can also be seen that two different block dimensions and beam dimensions corresponding to different theoretical accelerations for response are considered. The maximum stress values were obtained using the beam dynamics simulations and are summarized in Figure 11. Though the maximum stress values for the three designs are very similar for lower peak acceleration values, the differences between various designs increases with increasing acceleration. Among the three designs considered, Design 1 leads to the lowest maximum stress value and is likely to increase the threshold acceleration beyond which the structure fails. For example, at a peak acceleration of about $300 \times 10^3 \text{ g}$, Design 3 leads to a maximum stress that is a factor of 3 larger than that predicted for Design 1. In general, the maximum stress increases with decreasing value of beam width (b). It should also be noticed that the dependence of the maximum stress as a function of acceleration is pretty similar for all three designs. The rate of increase of maximum stress increases rapidly as can be seen in Figure 11 (note the log-log scale of the plot).

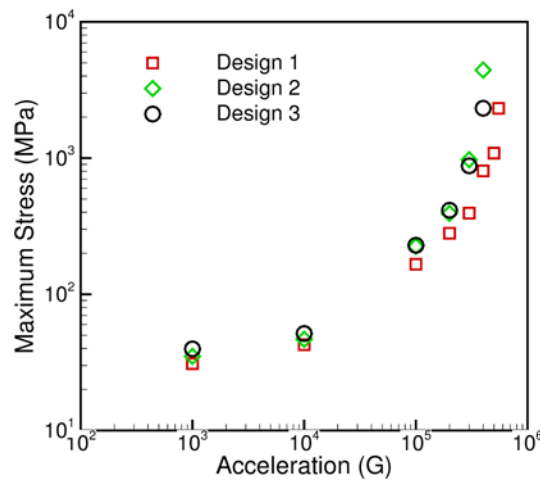


Figure 11: Comparison of absolute value of maximum stress predicted for various designs as a function of peak acceleration.

The analysis to study the dynamic effects was also performed on actual fabricated accelerometer dimensions as indicated in Table 2. Results are presented below for four different designs. Three of the accelerometer designs were for a threshold acceleration of 100 g and the fourth design responded to an acceleration of 150 g. Figure shows a summary of the maximum stress values for various peak acceleration values. It should be mentioned that the shape of the acceleration profile was same as that used for the earlier analyses. The results are qualitatively similar to results of Figure 5 (above) with the maximum stress being lesser than 1 GPa for all designs till the peak acceleration is about $1E5$ g. The design with the thinnest support beams fail the earliest which is consistent with our earlier analyses. The design with a theoretical response acceleration of 150 g survives for higher accelerations than the other beams. In general, the results indicate that a thinner beam, lighter block, and longer beam all result in lower threshold accelerations beyond which the beams fail.

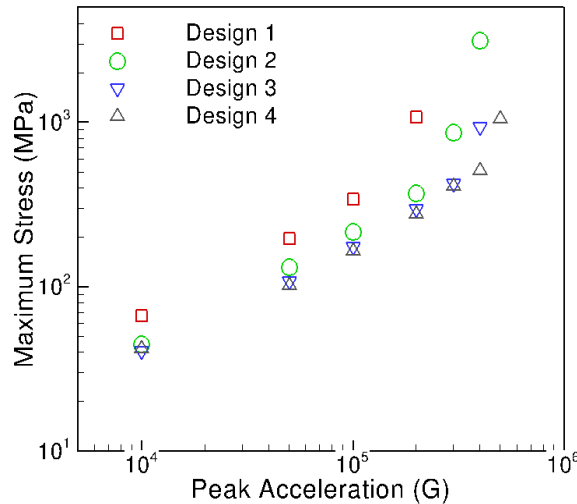


Figure 11: Comparison of absolute value of maximum stress predicted for fabricated designs as a function of peak acceleration.

2.1.6 Fabrication Process Flow

Using the above designed values, a fabrication process for the actual MEMS g-switches was developed. Fixed-fixed beams corresponding to the different acceleration levels were fabricated on SOI wafers with handle and device resistivity of $<0.01 \Omega\text{-cm}$ using standard micromachining techniques as shown in Figure 12. The first step in the Fabrication process involves the creation of lift-off mold on the bare SOI wafer. A metal layer of Cr/Au was then deposited and lifted off to create the contacts. In the next step, the SOI layer is patterned and etched using Deep Reactive Ion Etching (DRIE) to create the cantilevers. The final step in the fabrication process is the release of the cantilevers using controlled etching of the oxide using a mixture of HF and water in the ratio of 1:4. The released structures are carefully transferred to water and then transferred to solutions of Acetone, Methanol and then Isopropyl Alcohol for duration of 5 mins each. The samples are then dried using a Critical Point Drying (CPD) process.

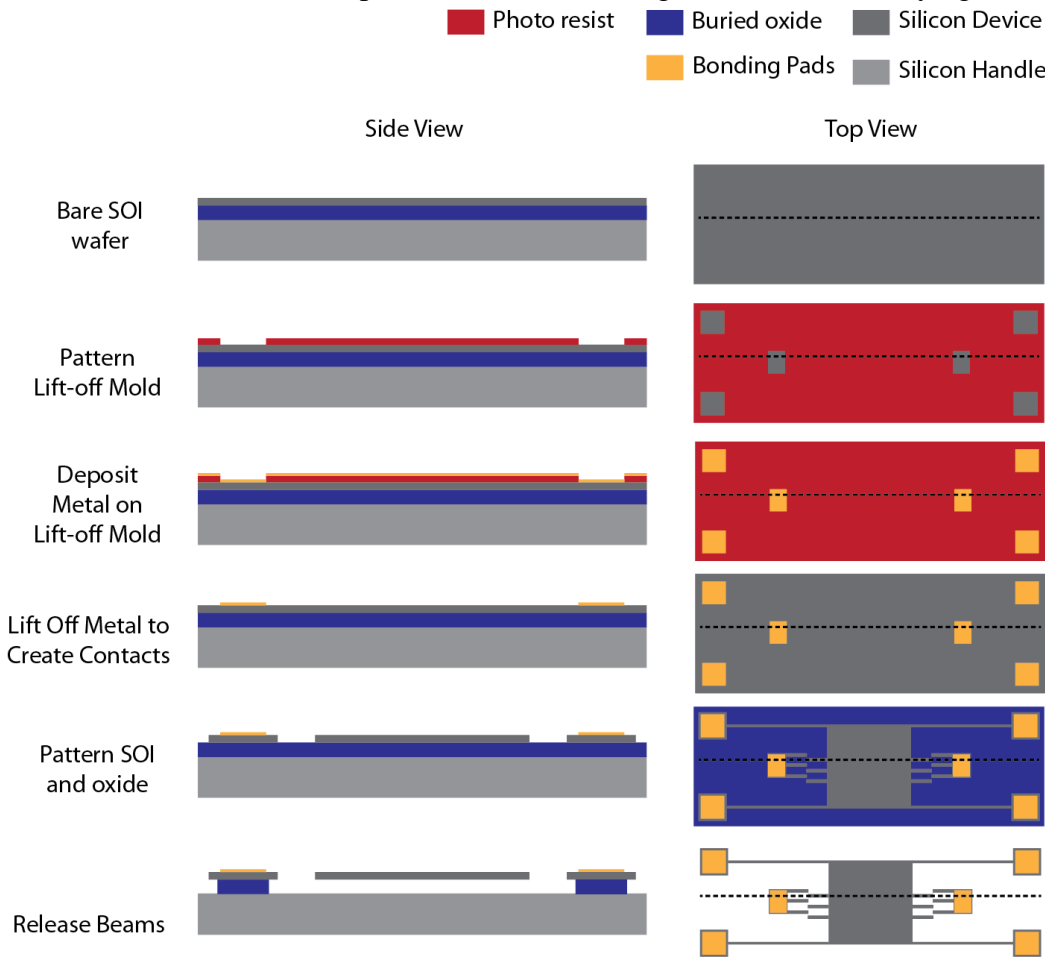


Figure 12: Optimized fabrication process

This fabrication process utilizes only 2 masks. It resulted in substantial higher fabrication yield (nearly all devices on a wafer were successful) and measurement repeatability.

Design Number	System Thickness (μm)	Block Width (μm)	Support Width (μm)	Support Length (μm)	Sensor Width (μm)	Sensor Length (μm)	Initial Gap (μm)
1 (Actual)	86.30	784.8	5.54	796.80	27	286.4	6.03
2 (Actual)	93.10	784.8	7.73	1064.9	27	286.4	6.03
3 (Actual)	100.0	784.8	8.80	1313.4	27	286.4	6.03
4 (Actual)	93.07	661.0	7.41	1110.0	27	286.4	6.03

Table 3: Measured dimensions of fabricated devices for the 100 g case

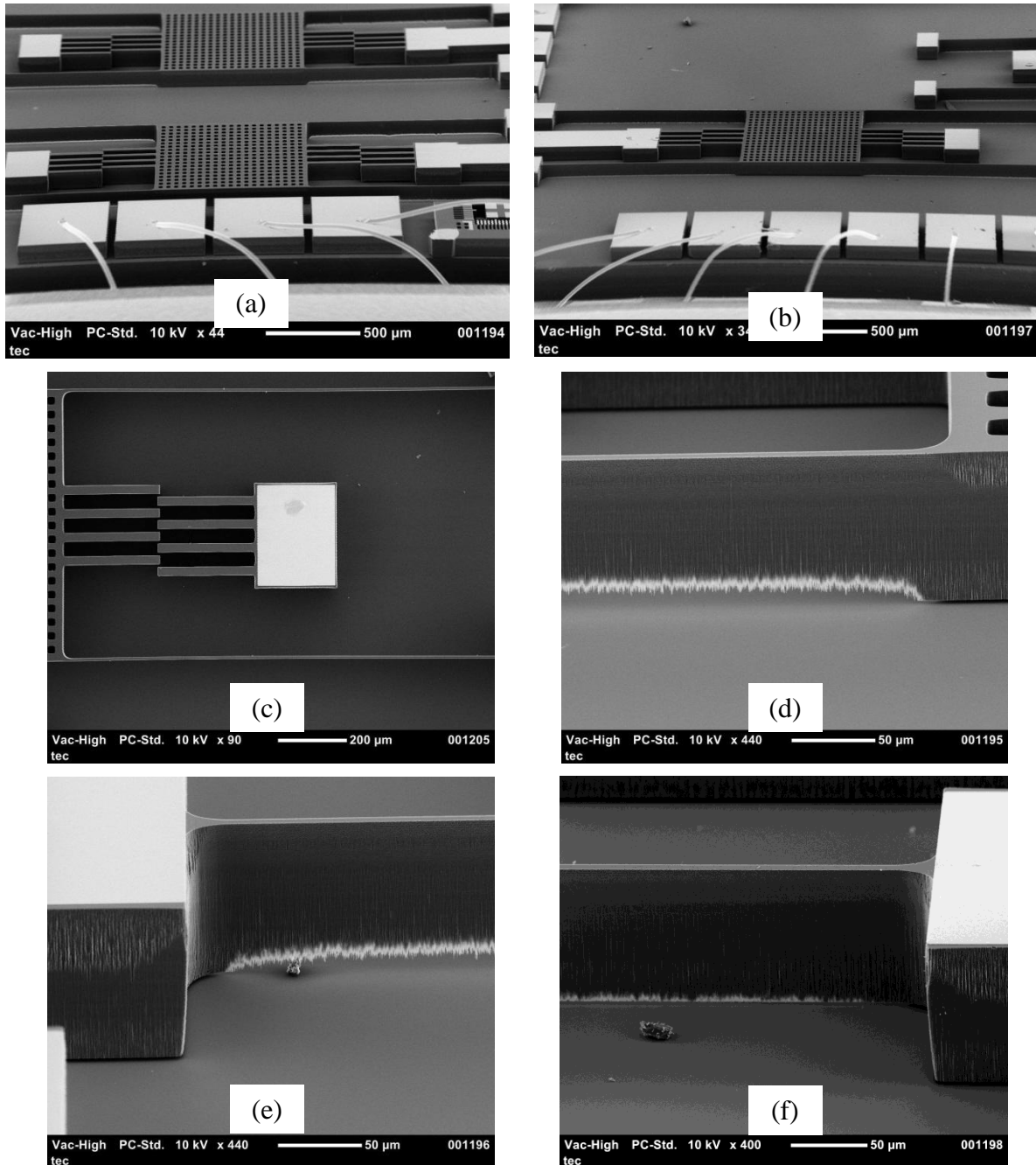


Figure 13: Fabricated g-switches using the optimized fabrication process. As it can be seen in the pictures there is a reduction in thickness of the support due to fabrication non-idealities

Beams were fabricated for three different support widths of 6 μm , 8 μm and 10 μm for a designed acceleration level of 100 g for a deflection of 5 μm . Figure 13 shows some of the devices fabricated using this process. Due to the fabrication non-idealities, especially during the Deep Reactive Ion Etching process where charge build-up occurs at the oxide layer, this results in undercutting of the supports as shown in Figure 13 (d) & (e). This results in a reduction of thickness in the supports, this effect is diminished as the thickness of the support increase as evident in Figure 13 (f).

These were then tested under low and high-g loads as explained in the experimental evaluation section. Table 3 shows the actual dimensions of the fabricated devices as determined using a Hitachi S-4800 scanning electron microscope. These dimensions are less than the designed due to fabrication uncertainties.

2.2 Experimental Evaluation

The experimental evaluation of the MEMS devices consists of the following steps 1) Packaging Process 2) Electrical Setup 3) Acceleration evaluation setup.

2.2.1 Packaging Process

A suitable packaging process was developed under the high-g program (HDTRA1-08-1-0026) to facilitate the testing of the MEMS devices under shock loads. In the first step of packaging process, the fabricated die is placed in a ceramic leadless chip carrier (LCC) package and wirebonded. This is then hermetically sealed using a gold-indium bonding ring on a glass lid. This package was then soldered onto a PCB with the electrical wire in place as shown in Figure 15. The soldered package was then placed in a tungsten package and potted with an encapsulating material. The encapsulating material consists of Stycast 1090 SI cured with catalyst 11 in the ratios and temperatures indicated in the technical data sheet. This potting material helps to reduce any unstable vibration on the device during impact testing as shown in Huang et. al [9].

2.2.2 Electrical Setup

Figure 14 shows a rough block diagram schematic of the electrical setup used for the measurement in the tests and the direction of the applied acceleration load in all test.. In all experiments, four devices of the same acceleration level are connected in parallel together and their combination is then connected through a 200 k Ω resistor (R_s) to 10 V power supply. The resistance (R_c) was then measured across the beam and the contact event which in this case is the sensing elements.

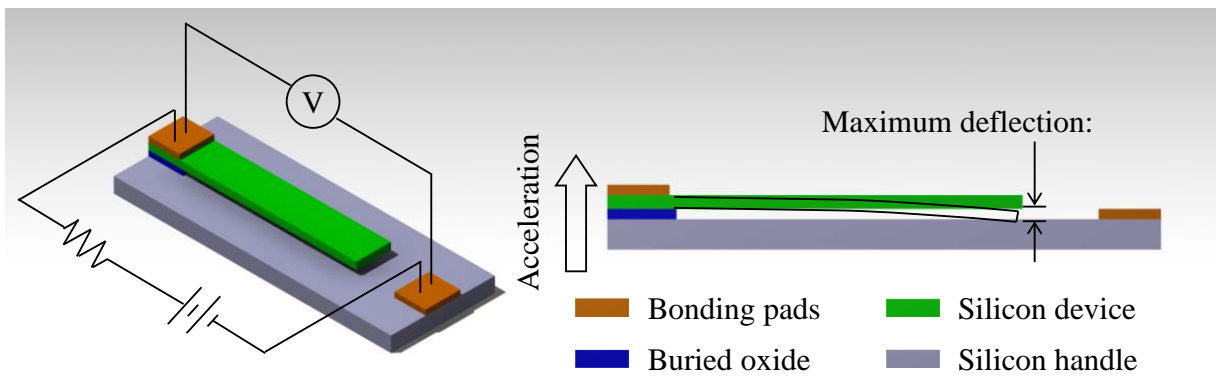


Figure 14: Schematic of the electrical setup used in all acceleration measurements

The packaged sample is connected to the electrical setup and subjected to low-g acceleration using a drop tower to determine the active transition region where the device begins to respond.

This is then subjected to impact acceleration using a modified Hopkinson bar setup. The details of both the low-g and high-g measurement setup are explained later in Section 2.5. Figure 15 shows an overview of the packaging process and the utilized measurement high-g setup and low-g setup

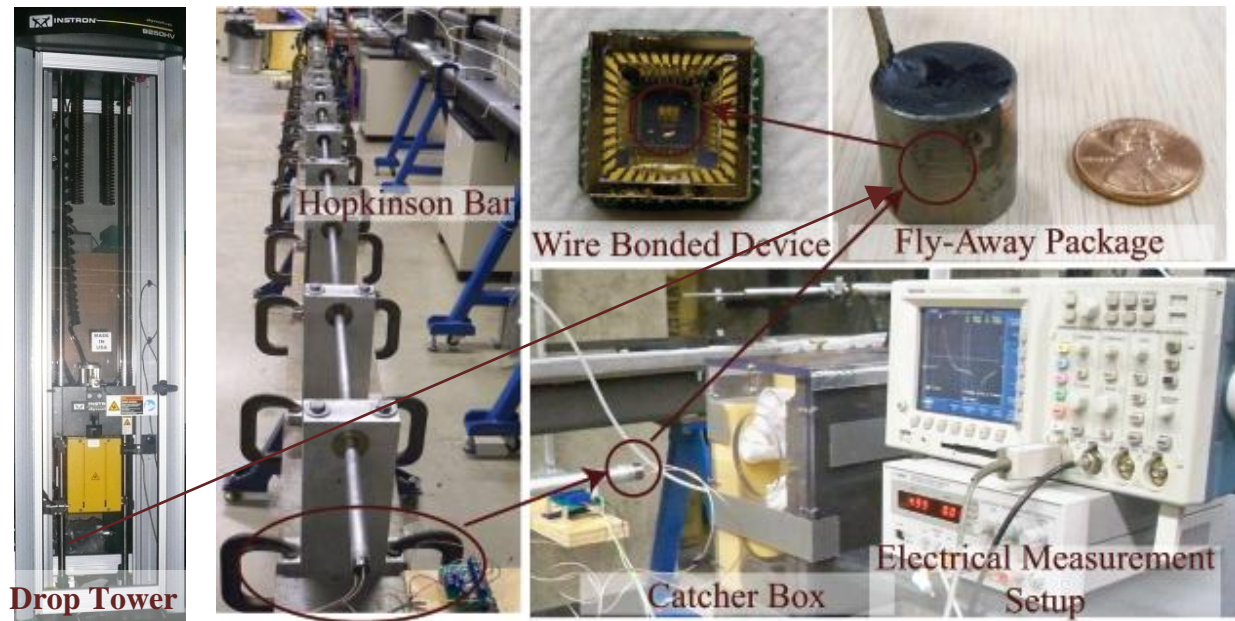


Figure 15: Packaging process and Hopkinson bar experimental setup

2.2.3 Experimental Results:

The fabricated devices were tested with the experimental setup described above. The average resistance (R_c) measured during the acceleration events was then found to be $\sim 133.3 \text{ k}\Omega$. Figure 16 shows the low-g devices of design type 1 ($6\text{-}\mu\text{m}$ wide beam) responding at low triggering at a low acceleration rate of 65.54 g for a peak applied profile of 97.13 g . The high contact resistance can be attributed to the small overlap area between the sensors.

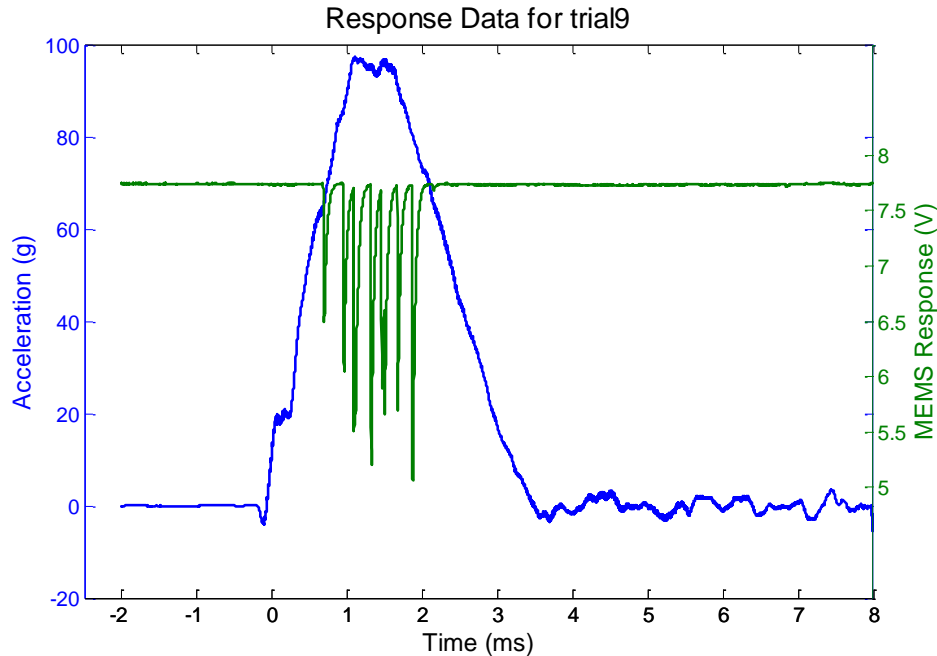


Figure 16: Successful measurement of a parallel combination of design type 1 ($6\text{-}\mu\text{m}$ wide) cantilevers triggering at 65.54 g for a peak applied profile of 97.13 g . Intermittent responses in MEMS response is due to contact bouncing

Figure 17 show the same devices responding at low triggering at a low acceleration rate of 68.77 g for a peak-applied profile of 100.4 g . In all experiments, the device shows a series of short duration of contact events which can be attributed to contact bouncing due to impact vibrations.

Figure 18 shows the lack of the response of the same device under a peak applied load of 52.57 g .

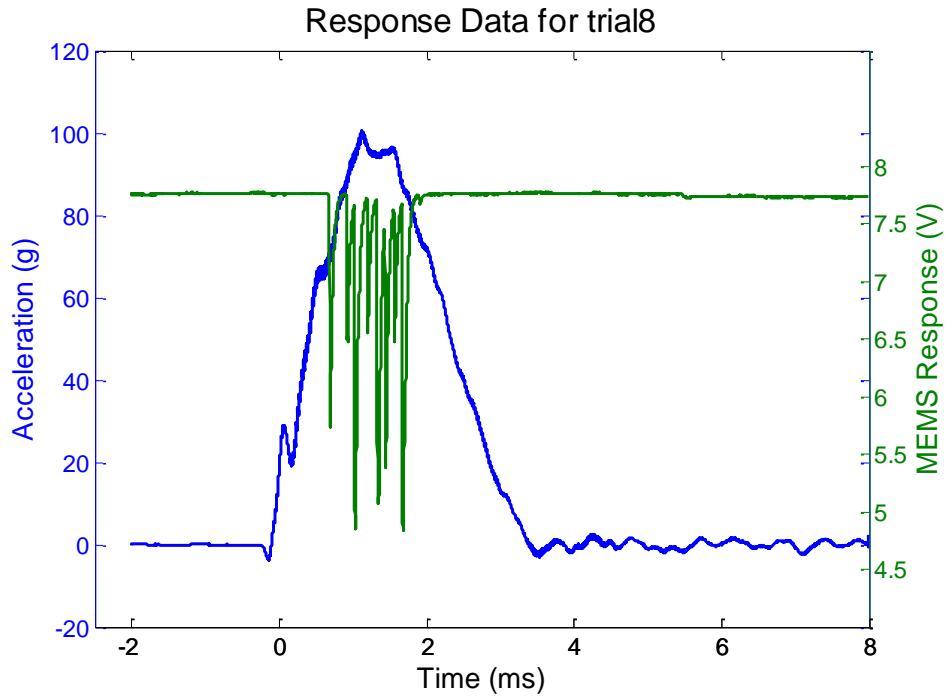


Figure 17: Another successful measurement of the same parallel combination of design type 1 ($6\text{-}\mu\text{m}$ wide) cantilevers triggering at 68.77 g for a peak applied profile of 100.4 g

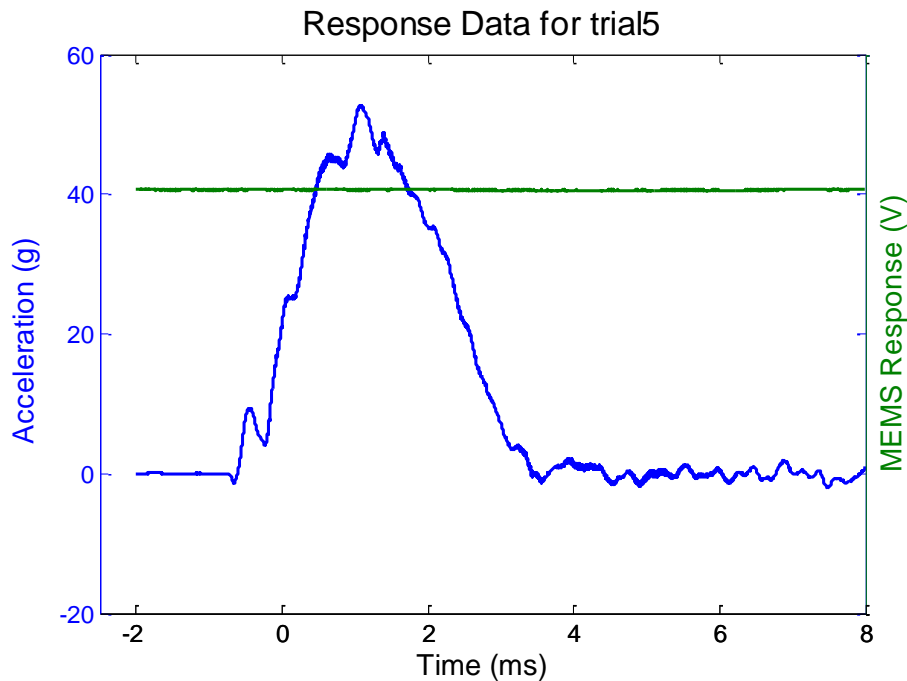


Figure 18: Successful measurement of the parallel combination of design type 1 ($6\text{-}\mu\text{m}$ wide) cantilevers under low acceleration conditions of 52.57 g. Since the acceleration is below the threshold acceleration there is a lack of response.

The device above was then subjected to a peak high-g acceleration profile of 20.560 g as shown in Figure 19 and then tested with the low-g measurement setup to determine functionality as shown in Figure 20.

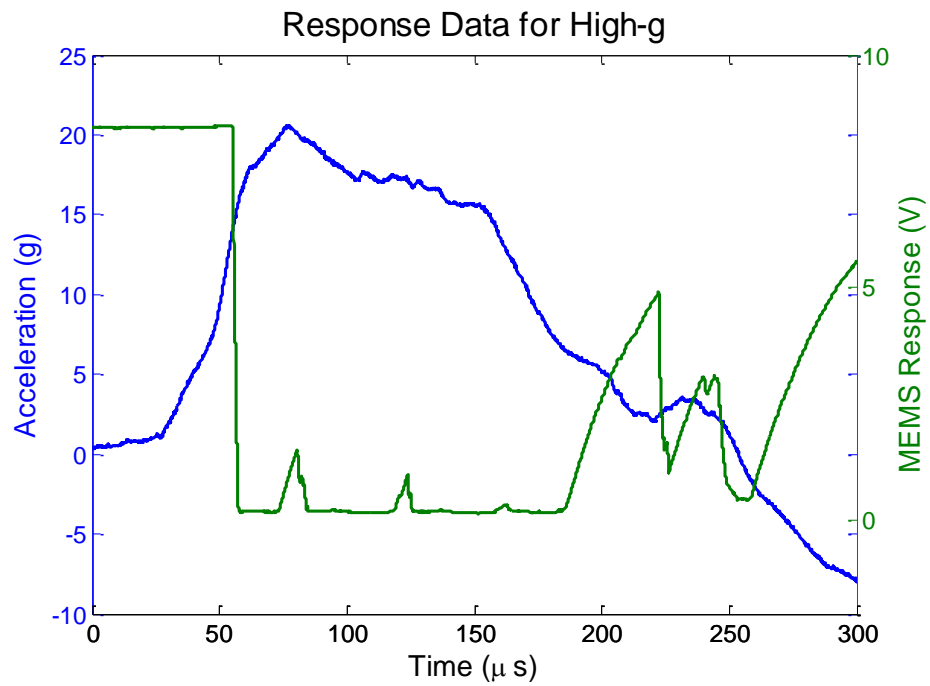


Figure 19: Parallel combination of design type 1 (6-μm wide) cantilevers under a peak applied acceleration profile of 20,560 g to check impact survivability

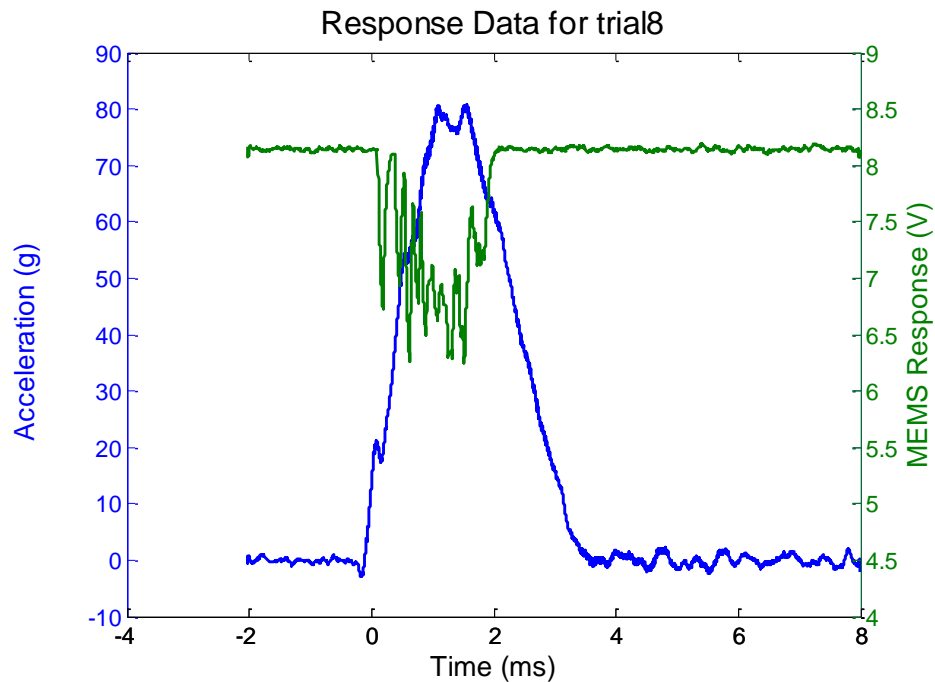


Figure 20: Parallel combination of design type 1 (6-μm wide) cantilevers under low acceleration conditions of 79.43 g. Device still triggers under low-g acceleration after applied impact acceleration indicating survivability.

The device finally failed after the applied profile shown in Figure 19 where a peak acceleration of 29,190 g was achieved

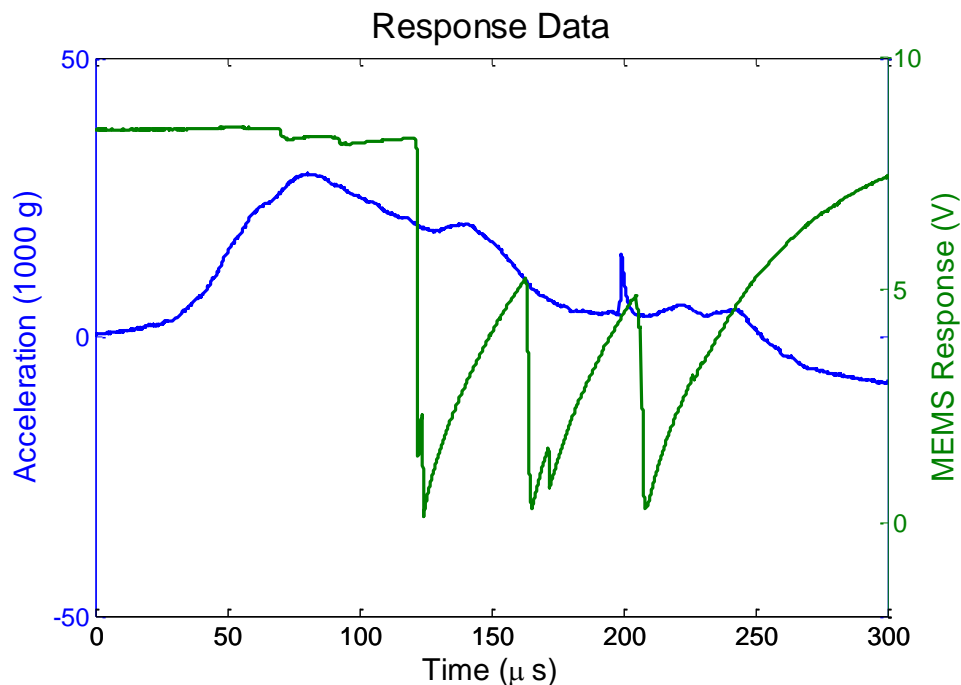


Figure 21: Parallel combination of design type 1 (6- μm wide) cantilevers under a peak applied acceleration profile of 29,190 g. The MEMS devices failed to respond to low-g acceleration after this applied load indicating failure.

As evident in the results, there is an indication of bouncing and some adhesions issues when contact occurs. Additional tests results are also available in Appendix A. However, there is a variation in detection range from their designed values; this can be possibly attributed to the approximations used in the design equations and the fabrication non-idealities especially at the anchor and the supports as shown in the fabrication process section. Additional research and testing is needed in this area to better quantify these results.

2.3 Simulation Comparison

Simulations of the block motion was conducted using a 1-D approach, approximating the system as a spring-mass-damper system. The block mass was assumed to be the effective mass for the system and the effective spring stiffness was obtained by the assuming a dual spring system by accounting for the stiffness of the sensor and support beams separately. The sensors would only cause a resistive force after the block displaced beyond the initial sensor gap. This essentially causes the block to experience a “soft stop,” allowing survivability at higher acceleration levels. The integration of the relevant equations of motion was performed using an RK-4 scheme. The results of the simulated motion are shown on the following pages.

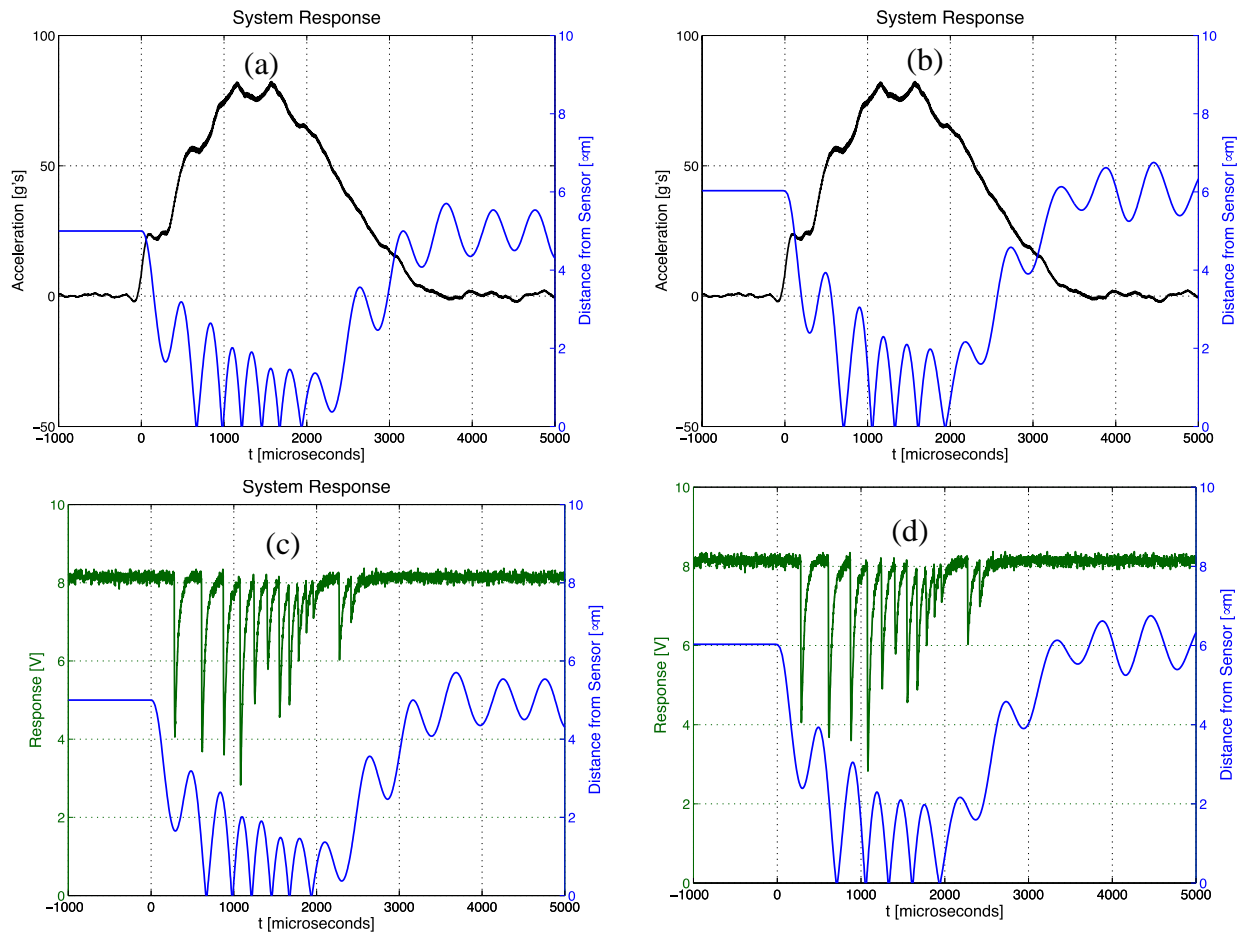


Figure 24: a) & b) Applied acceleration load with simulated displacement c) & d)Block displacement shown with the measured voltage for the Design 1 dimensions. Simulated displacement for the theoretical dimensions is shown on the left, displacement for the actual dimensions is shown on the right.

As can be seen in the previous images, system simulated system performance compares well with the observed response. The block oscillates initially, as is expected for an underdamped mass-spring-damper system. Design 1 was intended to respond to 100 g of acceleration, but due

to the initial oscillations, the simulated system contacts one period after the observed system. Unintended contact events such as this may be recognized by the frequency of the oscillations in the observed resistance.

As can be seen, the deviation from the intended dimensions due to the fabrication process does not significantly affect the motion of the system. Due to the variation, the actual device will be less sensitive to acceleration and thus takes slightly longer to contact and will more quickly release, but the difference is negligible when considering the overall motion.

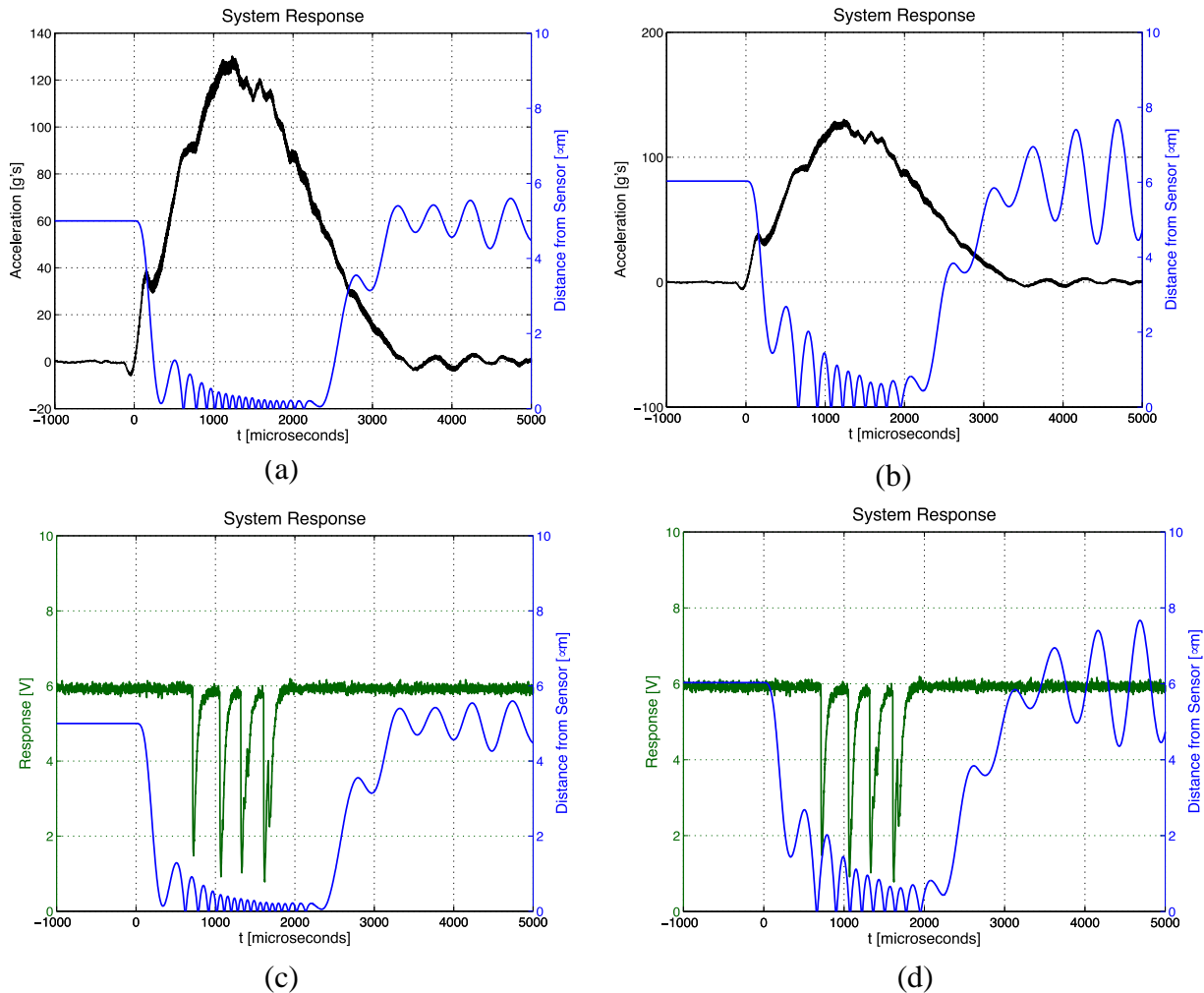


Figure 24: a) & b) Applied acceleration load with simulated displacement c) & d) Block displacement shown with the measured voltage for the Design 2 dimensions. Simulated displacement for the theoretical dimensions is shown on the left, displacement for the actual dimensions is shown on the right.

The above figures show the simulated displacement and observed response for Design 2. Similarly intended to respond at 100 g of acceleration, this design has thicker and longer support beams that theoretically yield the same stiffness. Due to the fabrication process, the characteristics of the system are slightly different.

Again, the differences between the theoretical and actual dimensions result in very similar performance. The system correctly contacts when the acceleration is near 100 g, and releases after the load decreases. Overall, the simulations and the observed response match much more closely than for the Design 1 simulations shown earlier.

Below are results for Design 2 when exposed to significantly higher acceleration loads. As can be seen, the simulated block quickly comes to rest against the sensors and remains there until the acceleration load decreases. The block does oscillate slightly, but the amplitude and frequency are relatively low compared to the lower g cases. The observed system response, however appears to indicate that the oscillations will cause sharp drops in resistance.

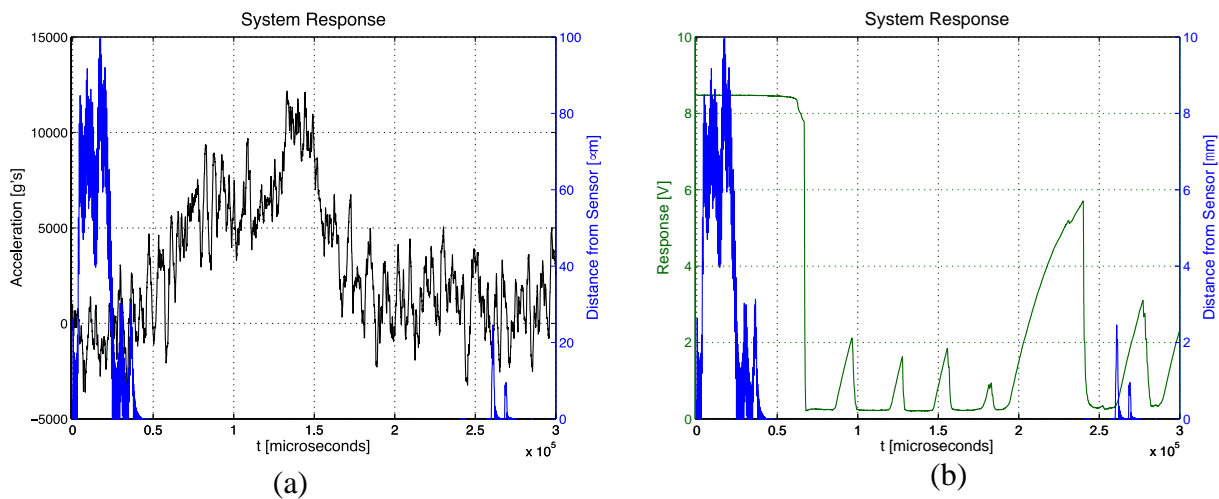


Figure 26: (a) Block displacement shown with the measured acceleration (left), (b) measured voltage (right) for the Design 2 dimensions exposed to high-g loading.

The following plots show low-g data for Design 3. This case is exposed to a higher peak acceleration than the low-g cases for Designs 1 and 2. Consequently, the simulated block experiences quicker contact and higher frequency bouncing. The actual observed response does not portray this higher frequency phenomenon.

Design 3 has the same intended response as the first 2 designs and has thicker and longer supports than Design 2. Again, the differences in simulated behavior due to the dimensions differences from fabrication do not ultimately affect the behavior.

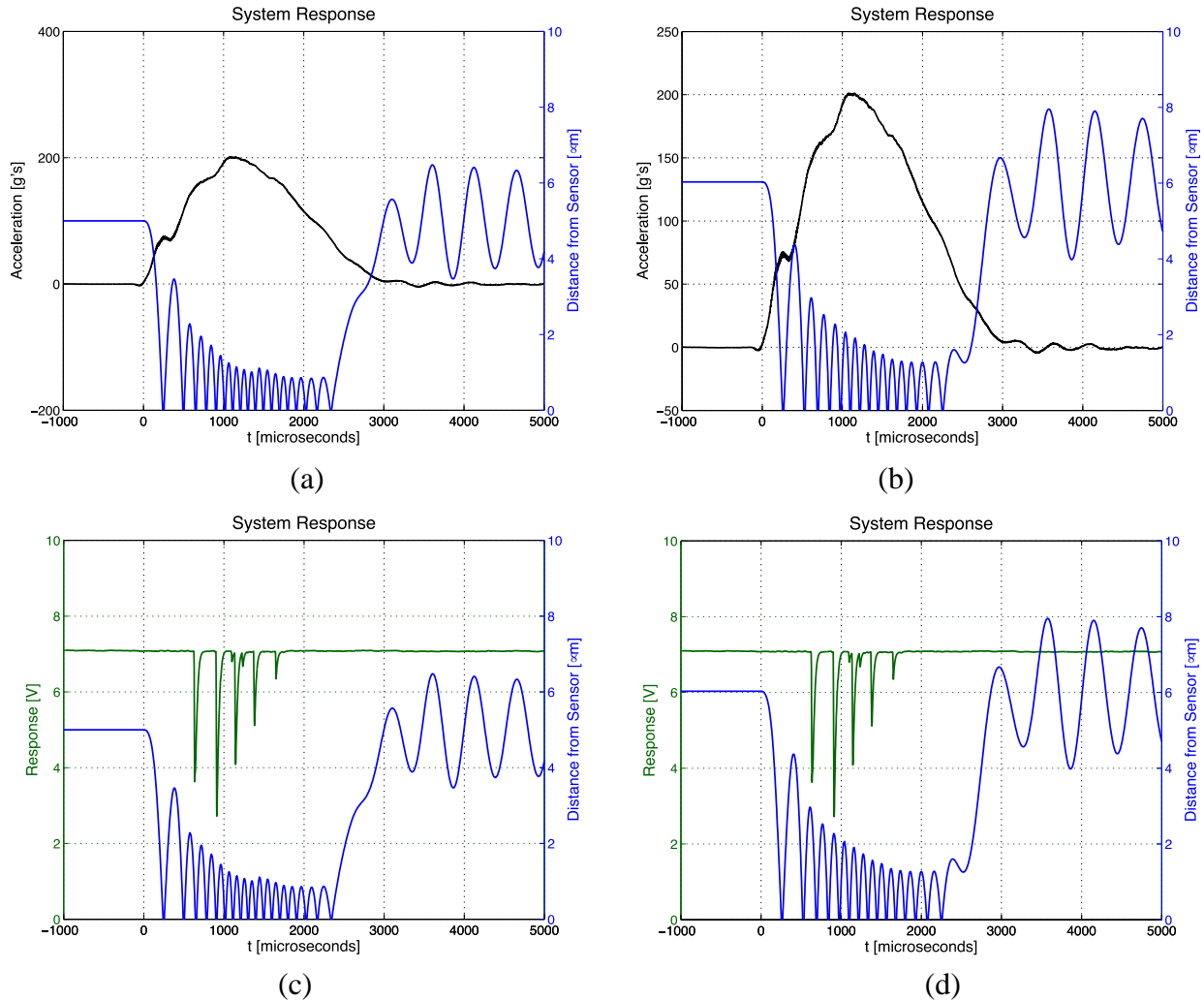


Figure 27: a) & b) Applied acceleration load with simulated displacement c) & d) Block displacement shown with the measured voltage for the Design 3 dimensions. Simulated displacement for the theoretical dimensions is shown on the left, displacement for the actual dimensions is shown on the right.

From the comparison of all the 100 g beam data, it is evident that the simulations best agree with the physically observed behavior when the systems experience the intended peak load, while deviation from that intended behavior leads to modeling error. If the expected response for a given device when properly accelerated is known, the data may be accurately reconstructed into the proper acceleration profile. Additionally, the simulations for the high-g case appear to demonstrate that the device will survive the higher loading, but the sharp resistance spikes warrant further investigation.

Below are results for Design 4, which is for a system intended to respond to 150 g of acceleration, with support beams most similar to Design 2. As can be seen, the difference between the theoretical and actual dimensions does not significantly affect the overall behavior.

The system experiences the highest frequency bouncing of the all the shown cases, and the observed resistance matches this behavior.

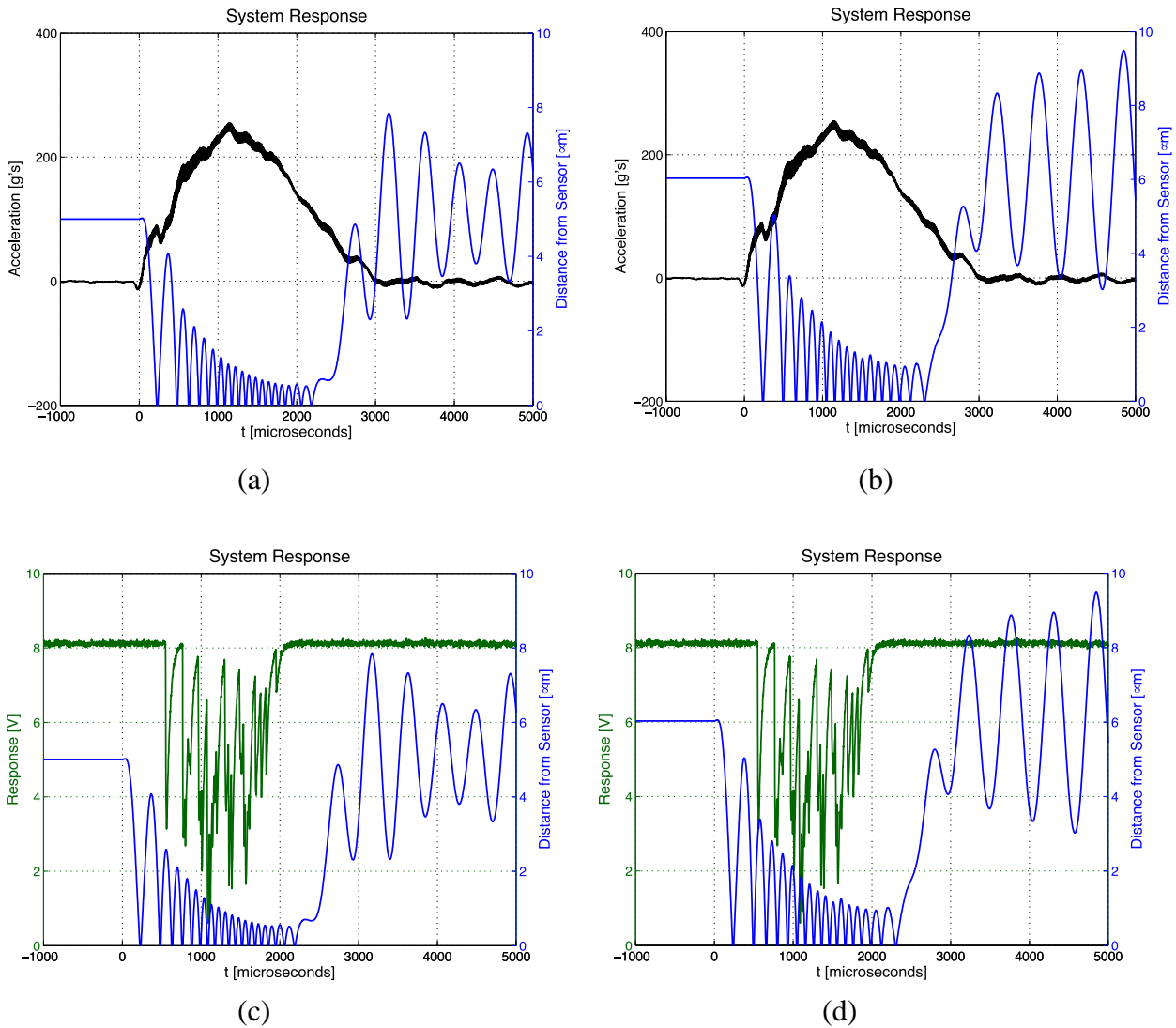


Figure 28: a) & b) Applied acceleration load with simulated displacement c) & d) Block displacement shown with the measured voltage for the Design 3 dimensions. Simulated displacement for the theoretical dimensions is shown on the left, displacement for the actual dimensions is shown on the right.

Overall, the 150 g simulation appears to capture all the observed behavior and the observed resistance drop and final return match the desired loads on the acceleration profile. Considering all the cases, the medium support beam width of approximately 8 μm seems to lead to the best agreement between the simulations and experiments, for both the 100 g and 150 g peak load designs.

2.4 Failure analysis

After the devices subjected to the acceleration profile, they were deputed and examined for possible causes of failure. This enables us to better design in the future. In Figure 29 (a) we can see that the failure occurring in the sensing elements due to a 45 degree shear. Similarly there is a 45 degree shear at the anchor, indicating a buildup of stress under high loads.

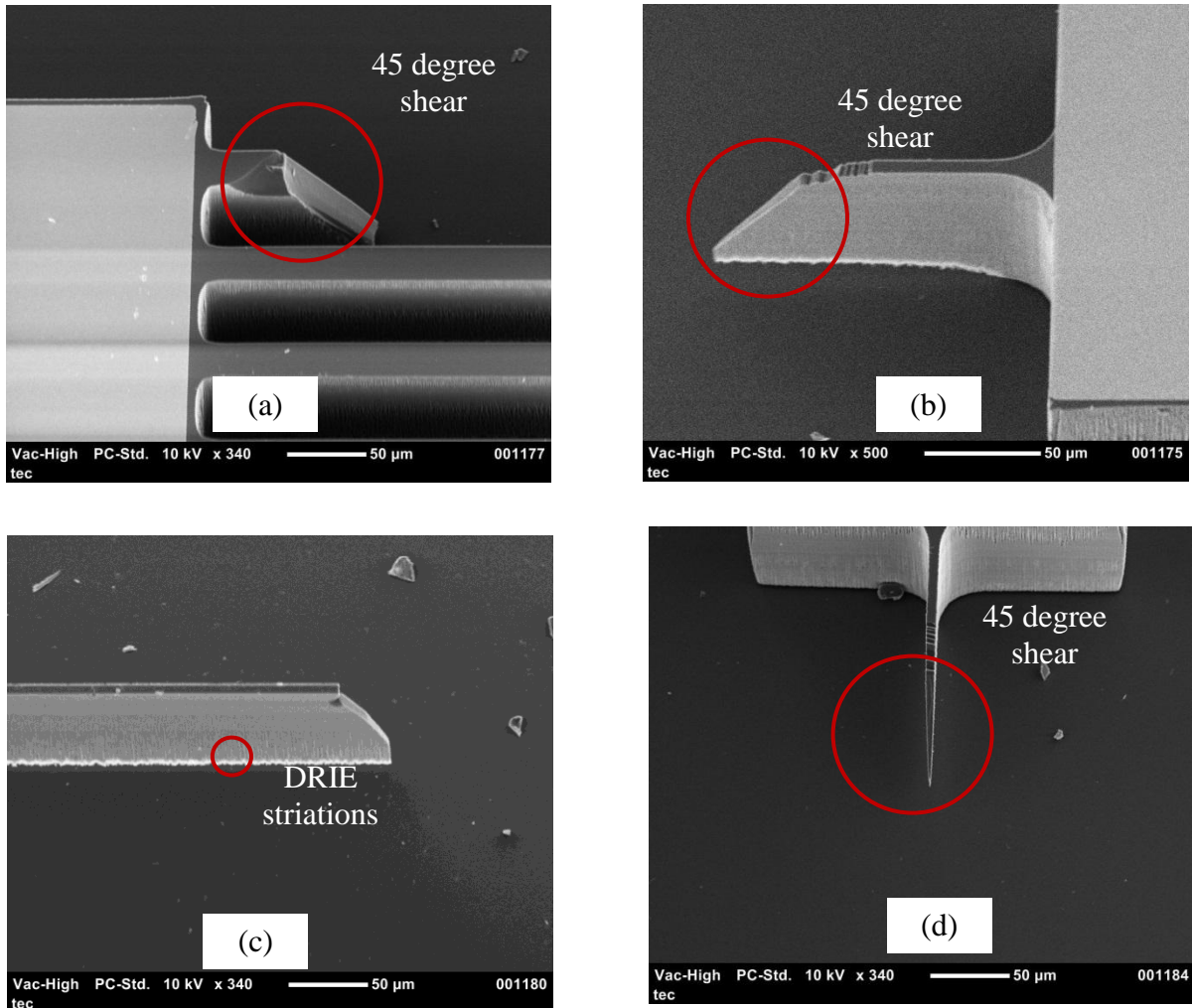


Figure 29: SEM images of tested devices. Devices show DRIE striation and 45 degree shears indicating possible failure points in the devices.

Figures 29(c) and (d) also show 45 degree shear where the support connects with the block and the shear break at the anchor.

Though the simulations have indicated survivability for acceleration ranges greater than 100,000 g, Experiment results have indicated that these devices have survived only up to an acceleration rate of ~20,000 g. Failure of these devices could be possibly attributed to the following causes:

- 1) Fabrication dimensions are less than the designed dimensions due to the fabrication limitations
- 2) Crack propagations due to striations caused by the DRIE process. (Figure 29(c))
- 3) Increased stresses in the support due to increased bouncing with the sensing elements.
- 4) Secondary vibrations caused by the test setup leading to the increased probability of failure.

In order to fully understand the causes of failure, further research needs to be conducted in this area.

2.5 Acceleration Evaluation setup:

In this section, we discuss the methods employed to create the controlled and predictable acceleration pulses that have been applied to the MEMS g-switches in order to evaluate their performance

The MEMS devices were evaluated by using the following experimental setups a) Drop tower tester (Figures 30 and 31) and b) Split-Hopkinson bar (Figures 32 and 33). As mentioned previously, low-g acceleration was imparted by the drop tower tester which was used to confirm the functionality of the MEMS g-switches. Then the survivability of the MEMS g-switches under high-g loads was evaluated using the split Hopkinson bar.

2.5.1 Low-g measurement Setup:

An Instron Dynatup 9250HV (Figure 21) was utilized for the drop tower tests. The fixture at the bottom of the drop weight carriage was redesigned for this project to accommodate both the external accelerometer (Meggitt/Endevco 7270A-2K)[13] and MEMS g-switch. The deceleration was created by the impact between the drop carriage and dead-stop mounted on the base plate of the drop tower tester.

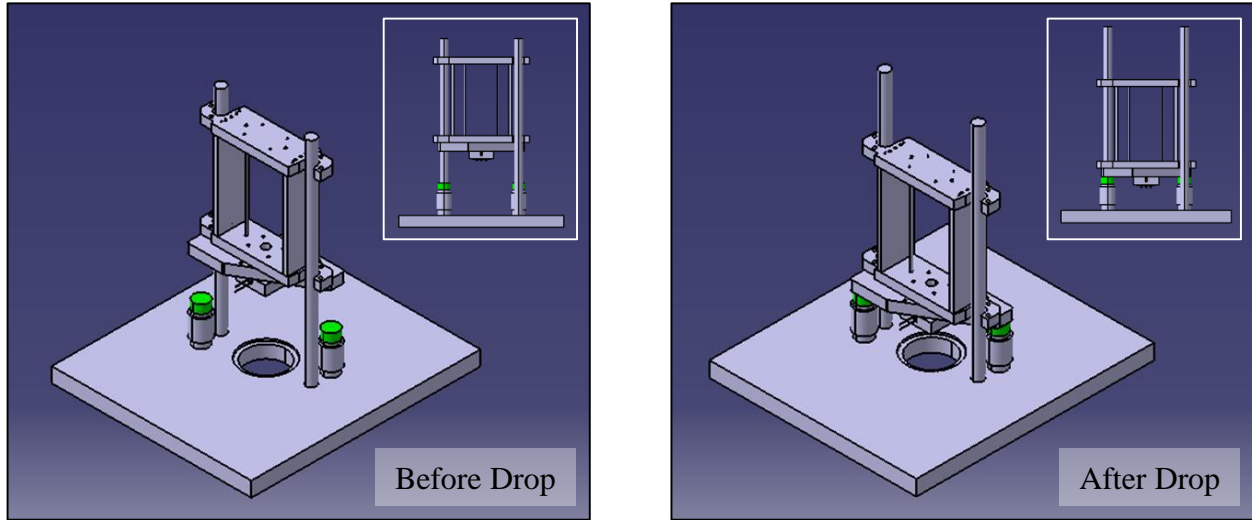


Figure 30: Drop tower tester – Overview

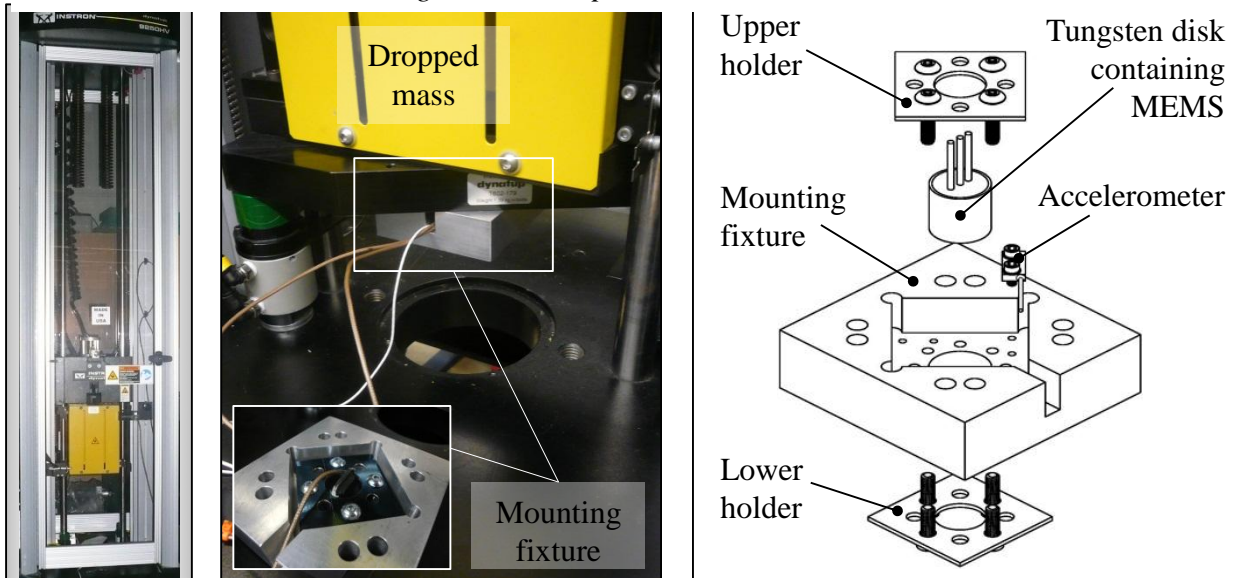


Figure 31: Drop tower tester – Details

2.5.2 High-g measurement Setup:

For the Hopkinson bar set up, an aluminum bar (diameter = 0.1905 m, length = 3.6576 m) was used as an incident bar, and a steel bar (diameter = 0.1905 m, length = 0.2794 m) was used as a striker and with a pulse shaper of annealed copper. Before each impact, the striker location was measured from the gas gun's opening surface to the leading edge of the striker bar. By varying gas gun pressure, the striker location and/or the thickness of the pulse shaper. For the strain gage on the incident bar, two strain gages were mounted in radial direction, 180 degrees from each other at the location 2.23 m from the boundary surface between the incident bar and the tungsten disk, which accommodates the MEMS g-switch inside. These two strain gages are the half-bridge of the Wheatstone bridge circuit, whereas the other half is located in the external half-bridge box. Together, these four strain gages make a complete Wheatstone bridge circuit. In the experiment, the following strain gages are used: Micro-Measurements, Part # WK-13-125BZ-10C, Gage Factor 2.08.

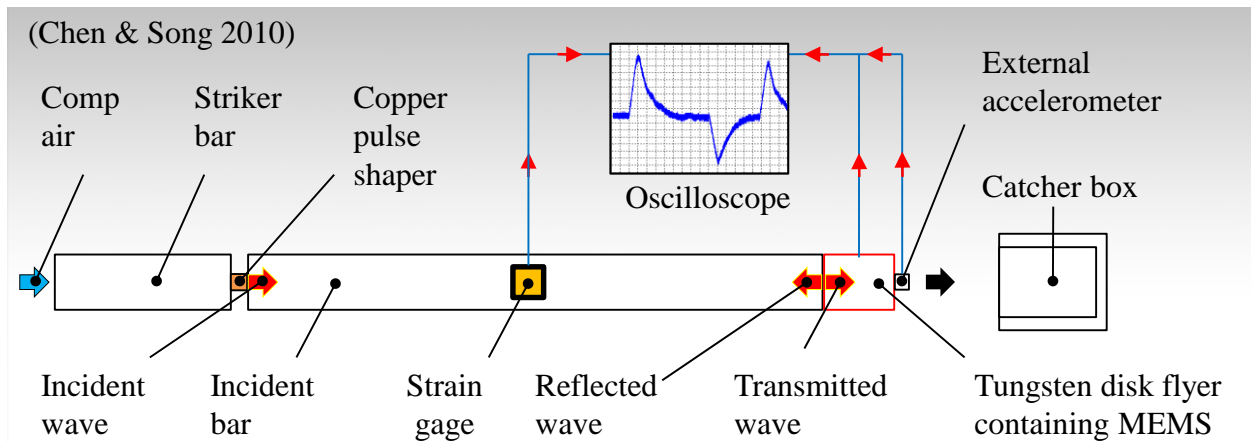


Figure 32: Hopkinson Bar setup – Overview

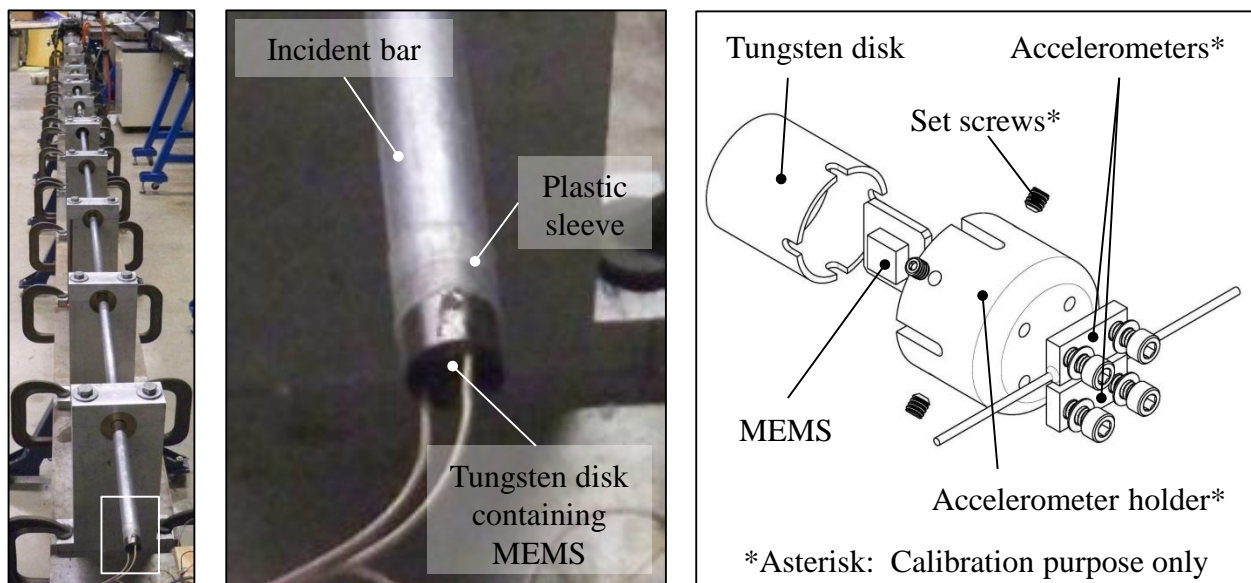


Figure 33: Hopkinson Bar setup – Details

A difficulty observed while setting up the experiment apparatus was the high level of the noise from the Endevco accelerometer. In order to minimize the noise from the Endevco accelerometer, the wiring scheme shown in Figure 34 was used as per the manufacturer’s instruction. In addition to the manufacturer instruction, the mesh that covers the four wires was used as the ground (GND) and connected to the GND for the power supply, as well as the differential pre-amplifier to reduce further electrical noise

By connecting all GND to the negative terminals of the electrical apparatus, it was possible to reduce the noise to about 0.25% of the stated capacity of the accelerometer. That is, since the stated capacity of the accelerometer was 2000 g, the noise level was about 5 g. Figure 35 shows the “tapping” test, where the accelerometer was gently tapped against a hard surface in order to verify the functionality of the accelerometer while the test set up was being evaluated.

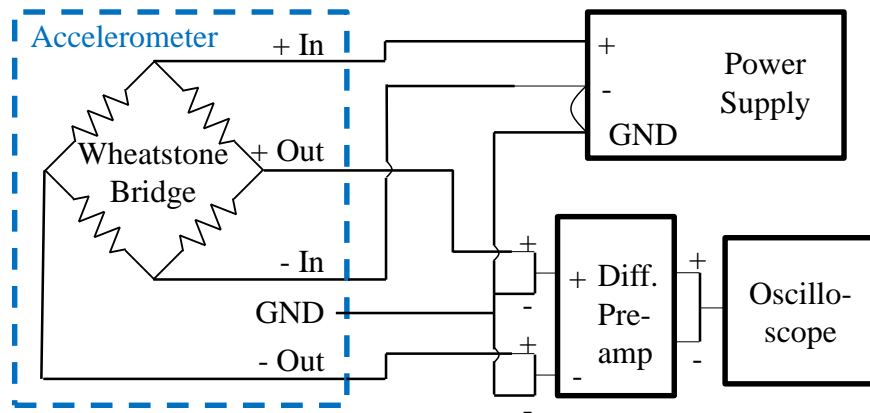


Figure 34: Endevco 7270A accelerometer electrical schematic

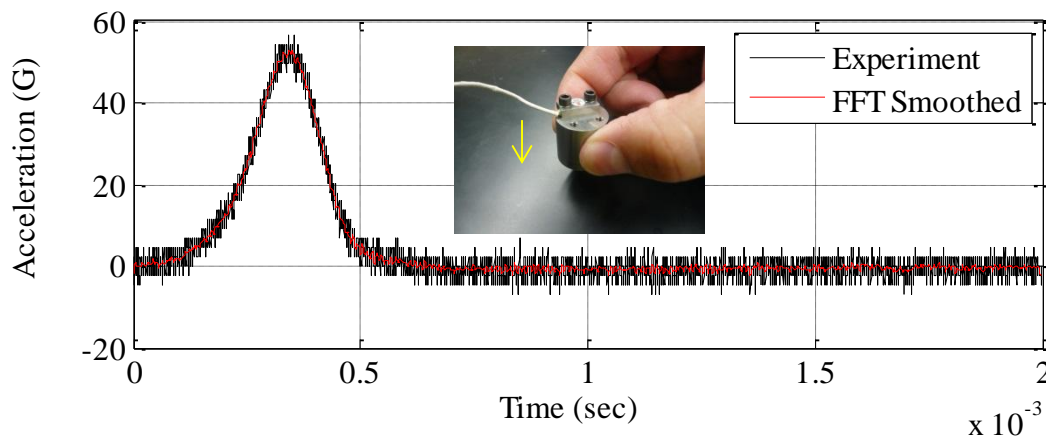


Figure 35: Accelerometer tapped against a hard surface as an initial verification

2.5.3 Experimental Procedure:

The experiment was conducted by first understanding the transition (switching) point using the drop tower tester. The transition point is the point where the MEMS beam makes contact with the switching surface, thus the electrical switches turns on and voltage potential across the MEMS device drops to zero or close to zero depending on the amount of the contact surface being sufficient or somewhat sufficient, respectively.

Since the beam was designed with particular g-value in mind, the point of interest was to see how close the experimental values are with respect to the experimental values (i.e. functionality) together with how much acceleration that the MEMS device survives (i.e., survivability). The following bullet points explain the specific procedures for each test.

Drop tower for MEMS functionality testing:

- Mount the MEMS device onto the drop tower fixture
- Start conducting experiment by dropping the fixture at low height (2 cm) and gradually increase the height to understand the transition (switching) point
- Make sure that the transition point is repeatable, as well as non-functionality below the transition point and functionality above the transition point are repeatable

Kolsky bar for MEMS survivability testing:

- Mount the MEMS device at the end of the incident bar
- Start conducting experiment by striking the striker to the incident bar at low pressure (10 psi) and gradually increase the pressure to understand the survivability of the MEMS device.

2.5.4 Potential sources of Experimental Error:

The experimental error appears to be larger at the lower gas gun pressure (Figure 39). The two potential sources of errors are inertia and friction of the striking bar inside the gas gun barrel. It is presumed that inertia and friction affect the consistency of striking velocity when the pressure is low (10 to 60 psi), thus lowering the reproducibility and causing errors that are inherent in low pressure test.

On the other hand, such effect becomes very small when the pressure is high (80 to 100 psi). Forrestal et al. (2002) [14] reported the effect of sabot mass, a sleeve around striker for snug fit and better alignment to the gun barrel, on the incident pulse, which also showed that the large sabot mass caused somewhat larger deviation from the analytical model based on Graff (1975). Therefore, it is presumed that when the gas gun pressure is low, the contribution from the friction and inertia is large, thus causing experimental error. When the gas gun pressure becomes high, on the other hand, the contribution from the friction and inertia is negligible.

2.5.5 Data Processing:

The experimental data processing from the drop tower tester is straightforward. The acceleration values were calculated directly from the output voltage values from the Endevco accelerometer. Also, the voltage drop from MEMS device is used to understand the transition point. Figure 36 shows both the acceleration profile and the voltage output from MEMS.

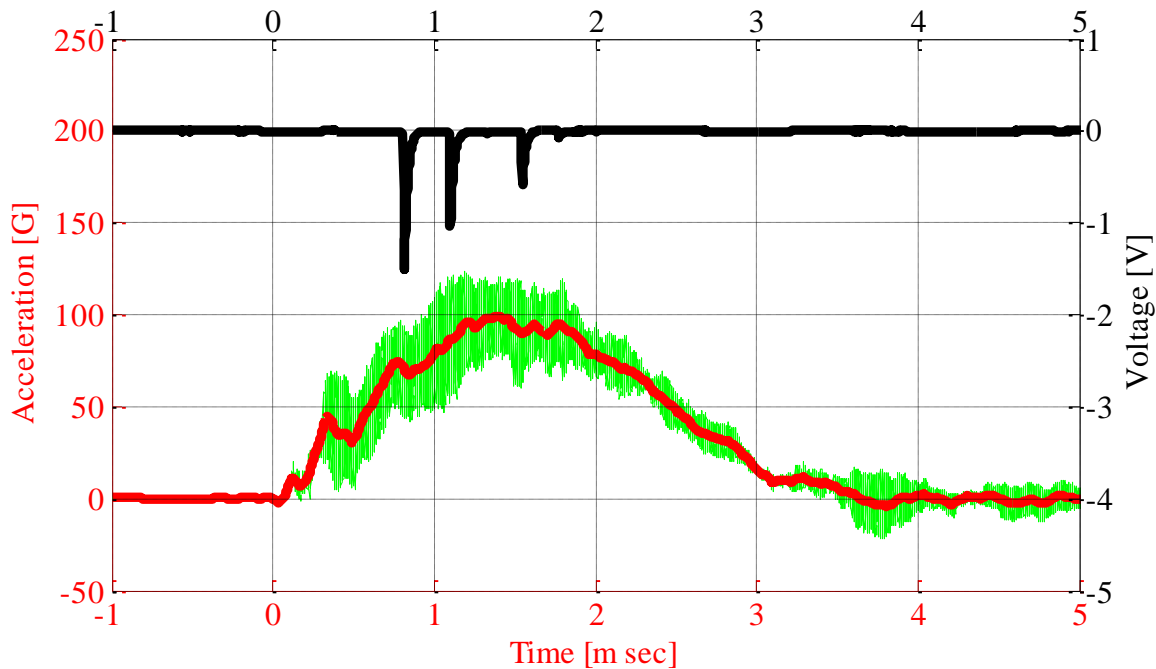


Figure 36: Example of test result from the drop tower tester.

The calculation of the acceleration from the accelerometer output voltage was conducted as follows: Each accelerometer has gage sensitivity number specified in the calibration certificates. The gage sensitivity number can be used to convert the output voltage into acceleration. For the Endevco accelerometer used (Model # 7270A-2K, Serial #F38986), the sensitivity was $88.48 \frac{\mu V}{G}$. Thus by simply dividing the output voltage by this sensitivity number resulted in the acceleration values. Acceleration is time dependent denoted by $a(t)$.

On the other hand, the data processing for the Kolsky bar experiment was more complicated. First, the incident and reflected pulse are recorded by the strain gage mounted on the incident bar. The pulses were used to calculate transmitted stress ($\sigma = E\varepsilon$). E is the Young's modulus of the incident bar material. The strain (ε) was calculated by the relationship $\varepsilon = \frac{2 V_{out}}{V_{in} S_g}$ based on Chen and Song, 2010[12]. Each term represents the following:

V_{out} = Time dependent output voltage from strain gage

V_{in} = Input voltage for Wheatstone bridge

S_g = Gage factor of strain gage

Now, the incident and reflected stress profiles are obtained (Figure 37). Next, the difference between the incident and reflected stress was calculated, where this difference was the stress profile that was transmitted to the tungsten disk, which contained the MEMS g-switch. By Newton’s second law, $F = ma$, acceleration profile (Figure 37) was calculated by $a(t) = \frac{F(t)}{m} = \frac{\sigma(t)A}{m}$. Each term represents the following (Foster et al., 2012) [17]:

- $\sigma(t)$ = Time dependent stress profile
- A = Cross – sectional area of the tungsten disk
- m = Mass of the tungsten disk

The assumption of the rigid-body motion was justified by Frew and Duong (2009)[18] as follows: a) the rise time of the incident stress profile in incident bar was long enough and b) tungsten disk length was short enough. In order to increase the length of the incident pulse duration for rigid-body motion, the steel striker bar and aluminum incident bar were used. This combination created the state of stress at the interface of the bars in compression consistently during the multiple reflection of wave in the striker bar (Foster et al, 2012 [17])

In addition to the stress and acceleration profile used during the experiment with pulse shaper, Figure 37 also shows these profiles without the use of the pulse shaper. The profiles in Figure 37 are based on the gas gun pressure of 53 psi. As shown in the stress profile plot without pulse shaper, the impedance difference between the steel striker bar and aluminum incident bar creates the “staged” or “stratified” appearance. In addition, high acceleration level was obtained without the use of pulse shaper. Figure 37 shows that the high acceleration of 90,000 g was obtained without the pulse shaper, whereas the same gas gun pressure resulted in about 30,000 g with pulse shaper.

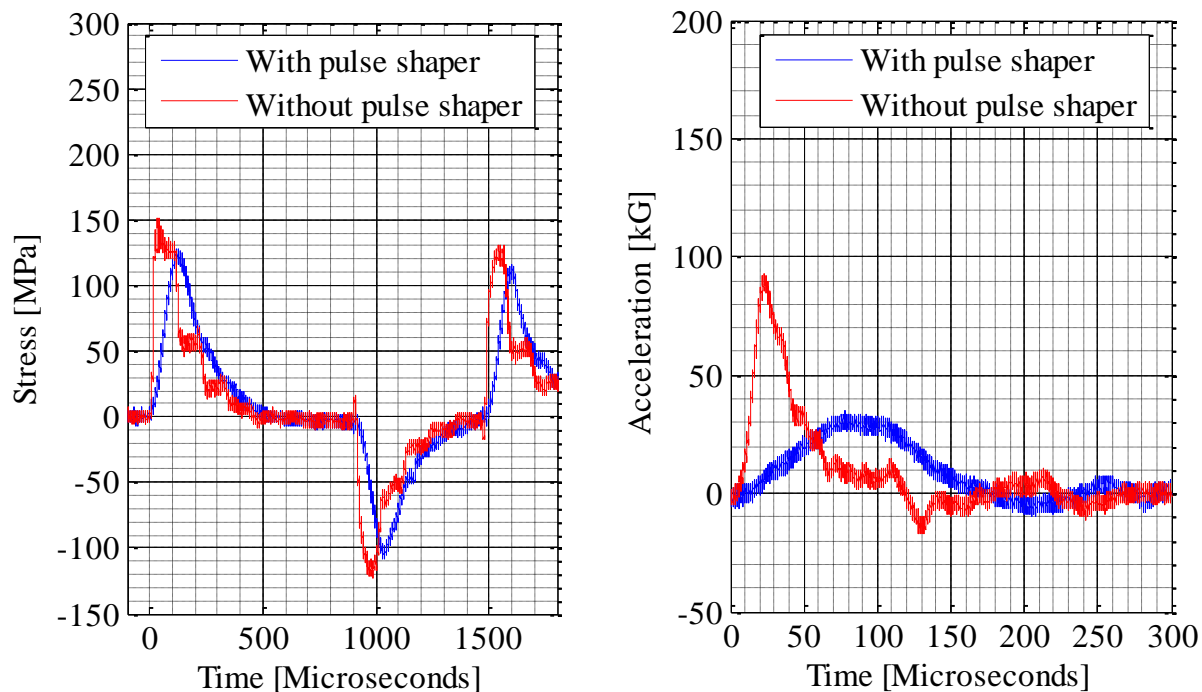


Figure 37: Example of test result from the Hopkinson Bar.

Figures 38 and 39 show the expected maximum acceleration using the drop tower and Hopkinson bar setups, respectively. For the drop tower setup, there is the direct relationship between the drop height and the maximum acceleration. For the Hopkinson bar experiment, there is also the direct relationship between the gas gun pressure and the maximum acceleration, together with the pulse shaper dimensions and the striker location, which is the distance from the gas gun opening surface to the leading edge of the striker bar

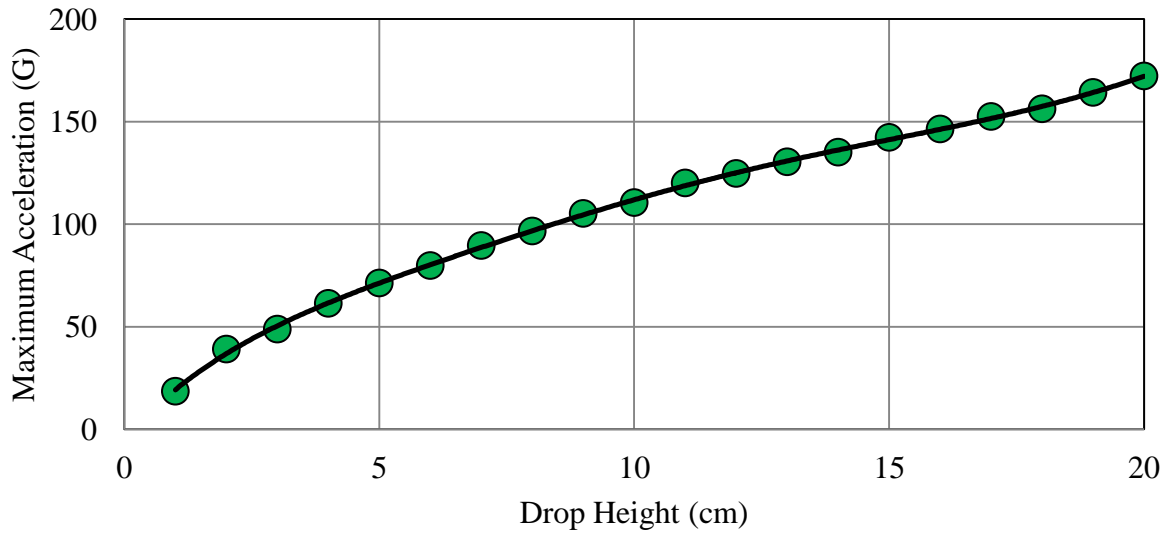


Figure 38: Maximum acceleration using the drop tower

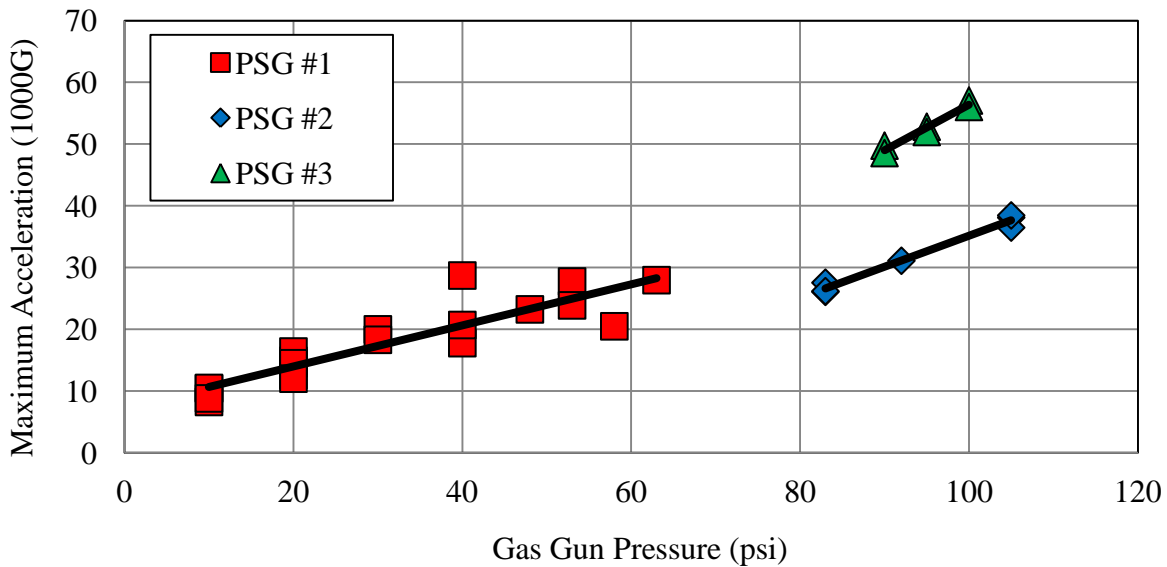


Figure 39: Maximum acceleration using the Hopkinson Bar

2.6 Concluding Remarks

In this study we have developed a design process for developing a g-switch capable of responding at low acceleration level (~ 100 g) and surviving impact loads of 100,000 g. In addition a process of evaluation of stress under high impact loads was developed. These designs have been fabricated using SOI wafers and are relatively stress free. Our measurements indicate that they can reliably result in on-resistance values of ~ 133 k Ω . The resistance is dependent on the overlap area of the sensing elements. The fabricated designs however were found to respond to lower acceleration of ~ 64 g and survive impact acceleration of $\sim 20,480$ g. The variations between the designed and the experimental response values can be attributed to the variation in the fabricated device dimensions. These responses have also been validated by the dynamic simulations. Further analysis is necessary to evaluate the failure of these devices and also to improve the design to make it more resistant to fabrication uncertainties. In addition, a low-g repeatable measurement setup using a drop tower to test MEMS device was developed. Preliminary results have shown the presence of bouncing and dynamic movement of the cantilevers under high-g and low-g loads.

2.7 Possible Future Directions

In order to better understand the bouncing phenomenon and the dynamic response of the beam the transient flexural wave propagation need to be well understood. This is especially important since the flexural wave length may become similar to, or shorter than, the thickness of the beam, which will add some complication to the wave motion. The necessity to understand the transient flexural wave motion in the microcantilever beam was confirmed through the following finite element analysis.

In the analysis, a microcantilever beam was modeled and analyzed in Abaqus/Explicit. The boundary conditions in Figure 40 were used together with the input acceleration profile based on Parkos et al. (2011) [22] in order to perform the dynamic analysis of beam deflection. The input acceleration profile and the observed flexural wave motion are shown in Figure 41.

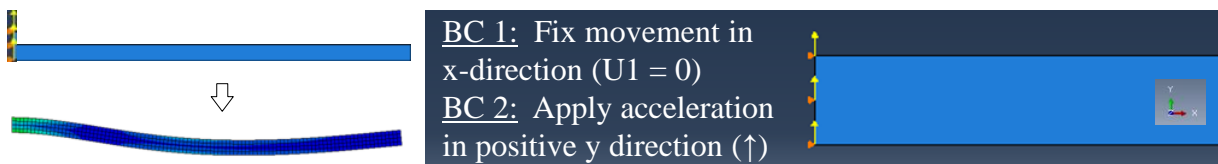


Figure 40: Boundary condition for finite element analysis

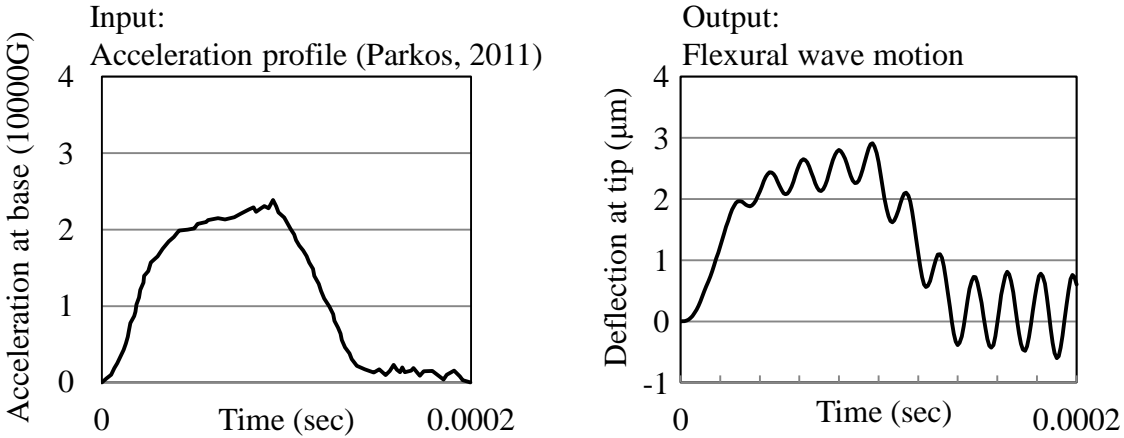


Figure 41: Finite element analysis result

From the experimental standpoint, the above high-g and low-g experiment can only be used to get the “on” and “off” response from the MEMS switch. Such information is, of course, useful from the standpoint of the development of the MEMS-g switch. However, in order to truly understand the dynamic response of the microcantilever beam, it is necessary to measure the instantaneous deflection upon impact using an optical measurement device, i.e., Laser Doppler Vibrometer (LDV).

In order to apply impact loading, a novel experiment apparatus must be developed. For this purpose, the researchers would like to propose a “miniature drop tower tester” as shown in Figure 42. In addition to a beam-alone set up, as shown in Figure 43, the apparatus can also be used to evaluate a beam-mass system. Furthermore, if two linear bearing are used simultaneously and the carriages in these bearings are coupled, the fixed-fixed beam with a mass located at the middle may be tested (Figure 43). Figure 44 shows the conceptual sketch of the miniature drop tower tester for the microcantilever beam. The proposed evaluation procedures for the microcantilever beam deflection are as follows:

- Drop the carriage contains the microcantilever beam from a known height (force)
- Calculate the expected maximum acceleration level from the Young’s modulus (E) of the dropped object, contact surface area (A), gravitational acceleration (g), drop height (d), height of the dropped object (h), and the mass of the dropped object (m) as follows:

$$Accel_{max} = \sqrt{\{E A g d\}/\{h m\}}$$
 per Endevco TP321 (2009)[13].
- Verify the maximum acceleration and acceleration profile using the accelerometer
- Measure the instantaneous deflection of the microcantilever beam using LDV
- Repeat the above to measure deflections at various locations to confirm the wave motion

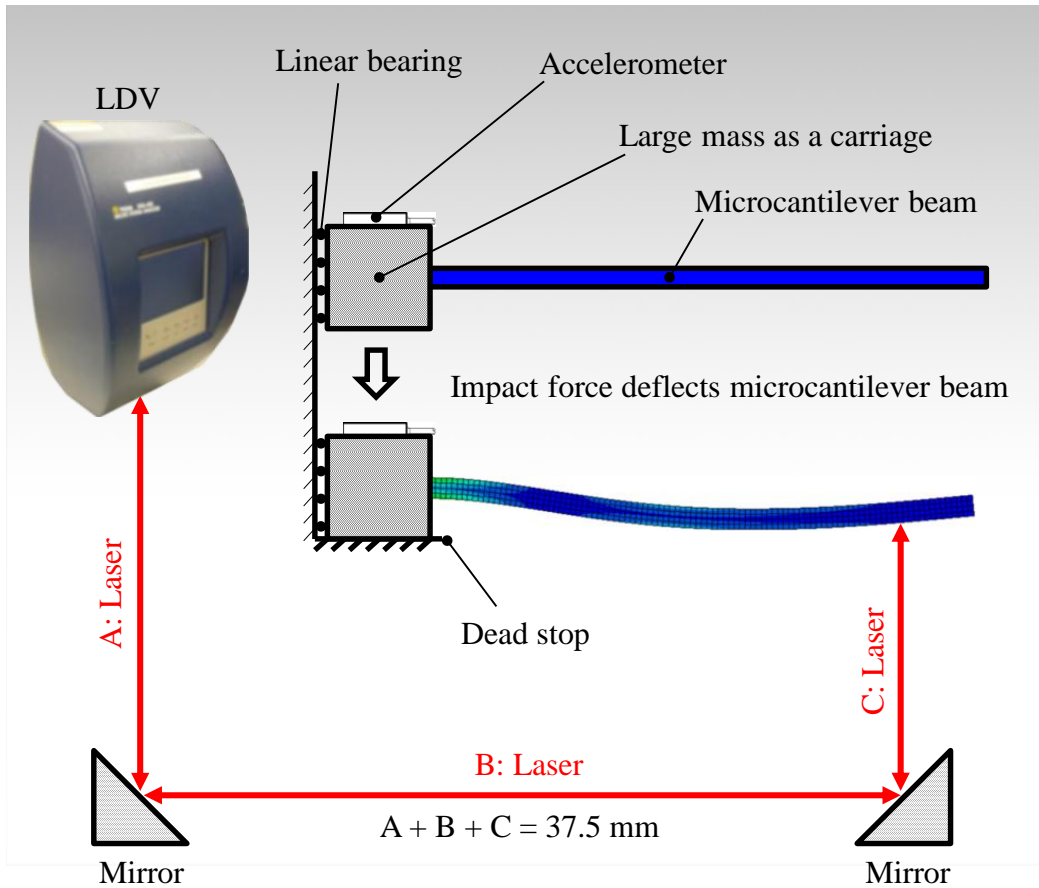


Figure 42: Deflection measurement of microcantilever beam

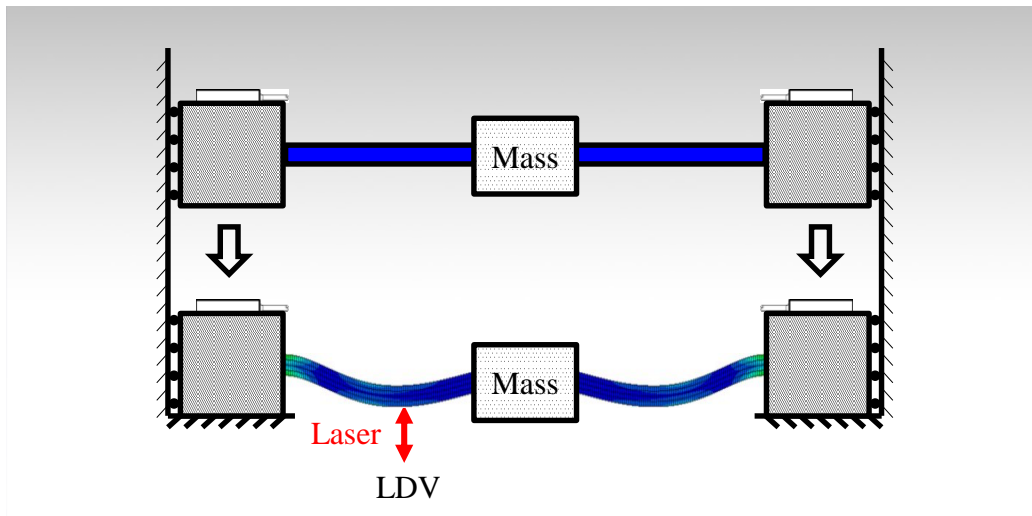


Figure 43: Fixed-fixed beam with a discrete mass located at the middle

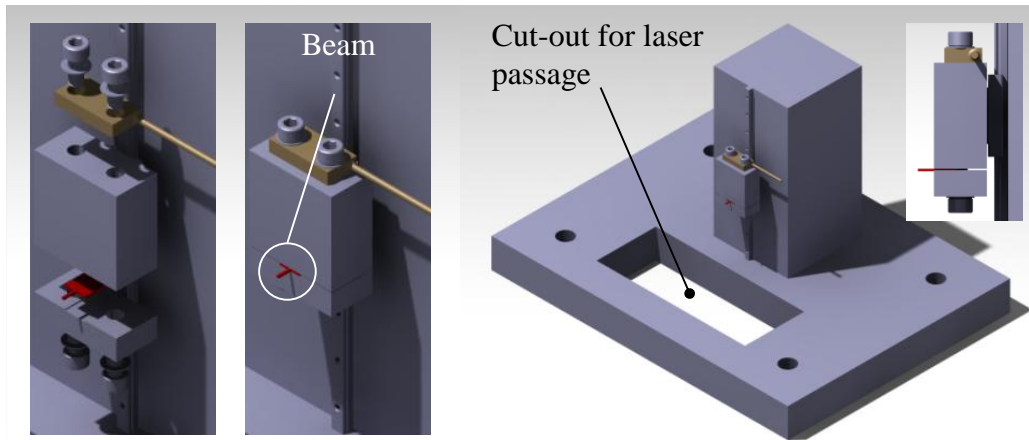


Figure 44: Conceptual design of miniature drop tower tester for microcantilever beam

- Future work on contact degradation both theoretically and experimentally under high-g loads needs to be performed in order to successfully model the contact behavior of the devices.
- Theoretical exploration of contact and structural degradation can be accomplished by researching the impact of stress-induced waves on the structure during high-g loads.
- Further work needs to be performed to create a full-fledged measurement system for detection of multiple levels simultaneously.

3. References

- [1] B. R. Davies, S. Montague, V.I. Bateman, F.A. Brown, R. Chanchani, T. Christenson, J. Murray, D. Rey, D. Ryerson "High-G Accelerometer for Earth-Penetrator Weapons Applications LDRD Final Report" Sandia National Laboratories, NM, Tech. Rep. SAND-98-0510, Mar.1998.
- [2] Beliveau, A.; Spencer, G.T.; Thomas, K.A.; Roberson, S.L.;, "Evaluation of MEMS capacitive accelerometers," *Design & Test of Computers, IEEE*, vol.16, no.4, pp.48-56, Oct-Dec. 1999
- [3] V. Bateman, N. Davie, and F. Brown, "Characteristics of a piezoresistive accelerometers in shock environments up to 150,000g," in *Institute of Environmental Sciences Proceedings*, Feb. 1995, pp. 290-294.
- [4] T. Togami, V. Bateman, and F. Brown, "Evaluation of a hopkinson bar fly-away technique for high amplitude shock calibration accelerometers," Sandia National Laboratories, NM, Tech. Rep. SAND-98-1444C, Nov.1988.
- [5] V. Srikar and S. Senturia, "The reliability of microelectromechanical systems (MEMS) in shock environments," *Microelectromechanical Systems, Journal of*, vol. 11, no. 3, pp. 206-214, June 2002.
- [6] J. Kimberley, I. Chasiotis, and J. Lambros, "Failure of microelectromechanical systems subjected to impulse loads," *International Journal of Solids and Structures*, vol. 45, no. 2, pp. 497-512, 2008.
- [7] D. V.-K. et. al., "Anelastic creep phenomena in thin metal plated cantilevers for mems," *Materials Science of MEMS Devices*, vol. 657, pp. EE2.5.1-2.5.6, 2001.
- [8] G. Rebeiz, *RF MEMS, Theory, Design and Technology*. John Wiley and Sons, 2003.
- [9] A.A. Alexeenko, S.F. Gimelshein, E.P. Muntz, A.D. Ketsdever, "Kinetic Modeling of Temperature-Driven Flows in Short Microchannels," *International Journal of Thermal Sciences*, Vol. 45, No. 11, Nov. 2006, pp. 1045-1051.
- [10] X. Guo and A. Alexeenko, "Compact Model of Squeeze-Film Damping based on Rarefied Flow Simulations," *Journal of Micromechanics and Microengineering*, Vol. 19, No. 4, April 2009, 045026.
- [11] M. A. Gallis M A and J. R. Torczynski, "An Improved Reynolds-equation Model for Gas Damping of Microbeam Motion", *IEEE/ASME Journal of Microelectromechanical Systems*, Vol. 13, pp. 653-659, 2004.
- [12] W. Chen & B. Song (2010). Split Hopkinson (Kolsky) Bar. New York, NY: Springer.
- [13] Endevco Technical Paper. (2009). Acceleration levels of dropped objects. TP321. 20700 Rancho Viego Road, San Juan Capistrano, CA.
- [14] M.J. Forrester, D.J. Frew, & W. Chen, (2002). The effect of sabot mass on the striker bar for split Hopkinson pressure bar experiments. *Experimental Mechanics*, 42 (2), 129-131.
- [15] M.J. Forrester, D.J. Frew, J.P. Hickerson, & T.A. Rohwer, (2003-a). Penetration of concrete targets with deceleration-time measurements. *International Journal of Impact Engineering*, 28, 479-497.
- [16] M.J. Forrester, T.C. Togami, W.E. Baker, & D.J. Frew, (2003-b). Performance evaluation of accelerometers used for penetration experiments. *Experimental Mechanics*, 43 (1), 90-96.
- [17] J.T. Foster, D.J. Frew, M.J. Forrester, E.E. Nishida, & W. Chen, (2012). Shock testing accelerometers with a Hopkinson pressure bar. *International Journal of Impact Engineering*, 46, 56-61.

- [18] D.J. Frew, & H. Duong, (2009). A modified Hopkinson pressure bar experiment to evaluate a damped piezoresistive MEMS accelerometer. SEM Proceedings 2009, 1896-1903.
- [19] K.F. Graff, (1975). Wave motion in elastic solids. Mineola, NY: Dover. Originally published by Ohio State University Press.
- [20] T.C. Togami, W.E. Baker, & M.J. Forrestal,(1996). A split Hopkinson bar technique to evaluate the performance of accelerometers. Journal of Applied Mechanics, 63 (2), 353-3563
- [21] D. Parkos, N. Raghunathan, A. Venkattraman, A. Alexeenko,, & D. Peroulis, (2011). Near-contact damping model and dynamic response of micro-beams under high-g loads, IEEE MEMS, 465-468.
- .

4. Appendix A

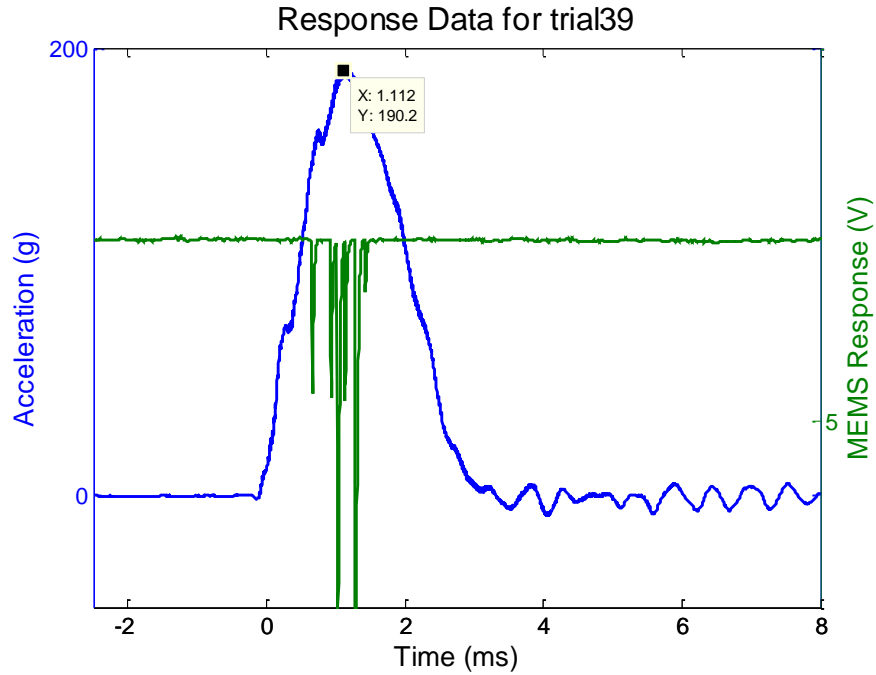


Figure 1: Successful measurement of the parallel combination of design type 3 (10- μ m wide) cantilevers triggering at 148.9 g for a peak applied profile of 190.2 g

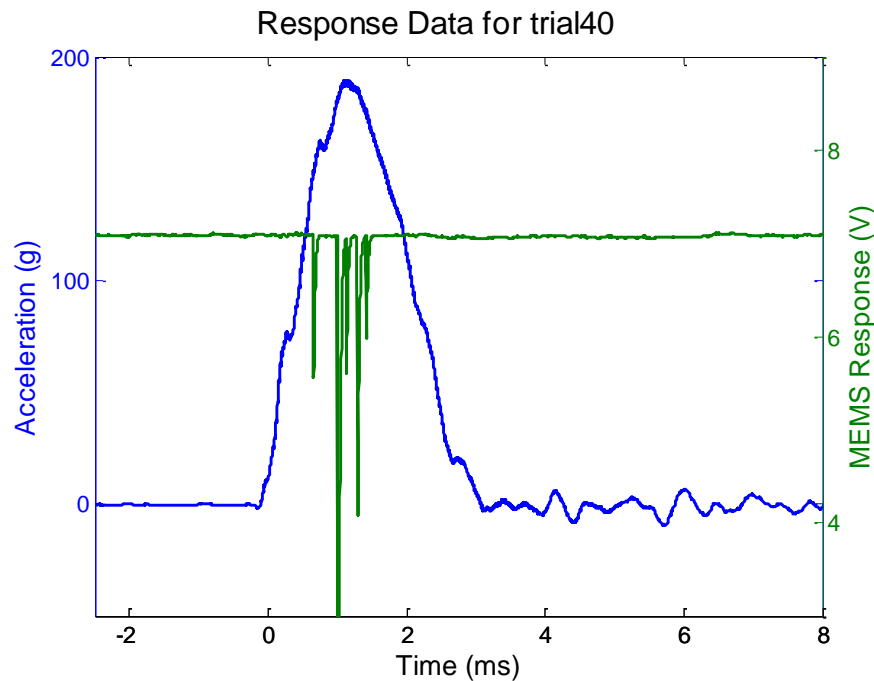


Figure 2: Successful measurement of the parallel combination of design type 3 (10- μ m wide) cantilevers triggering at 145.7 g for a peak applied profile of 187.3 g

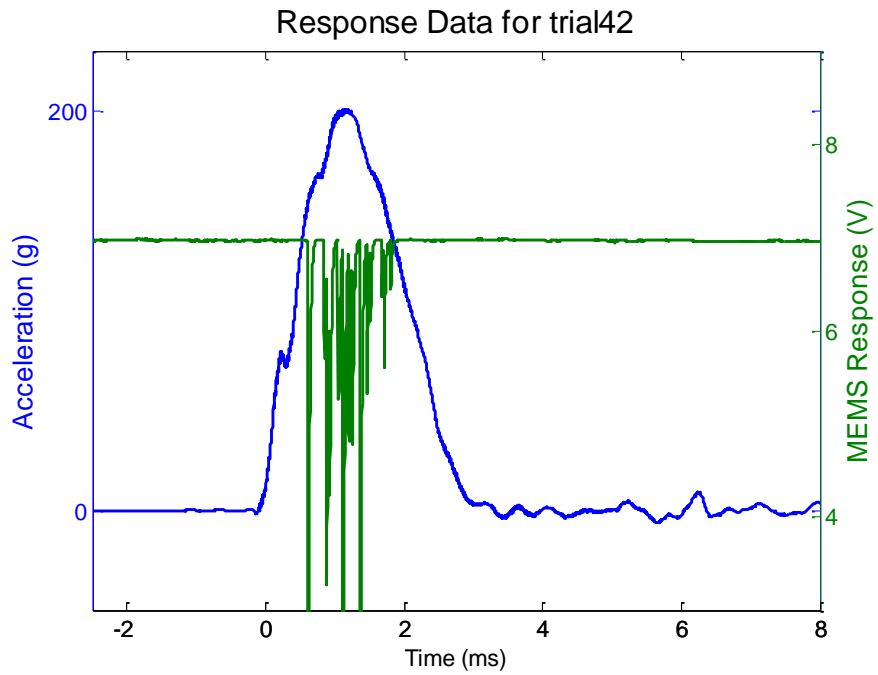


Figure 3: Successful measurement of a parallel combination of design type 3 (10- μm wide) cantilevers triggering at 153.9 g for a peak applied profile of 200.8 g

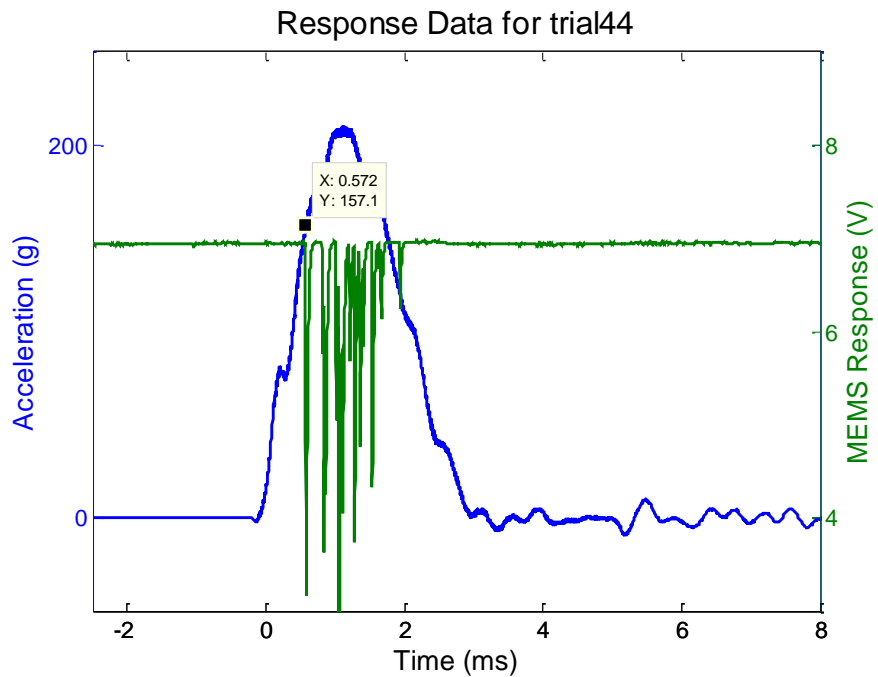


Figure 4: Successful measurement of Parallel combination of design type 3 (10- μm wide) cantilevers triggering at 157.1 g for a peak applied profile of 209.9 g

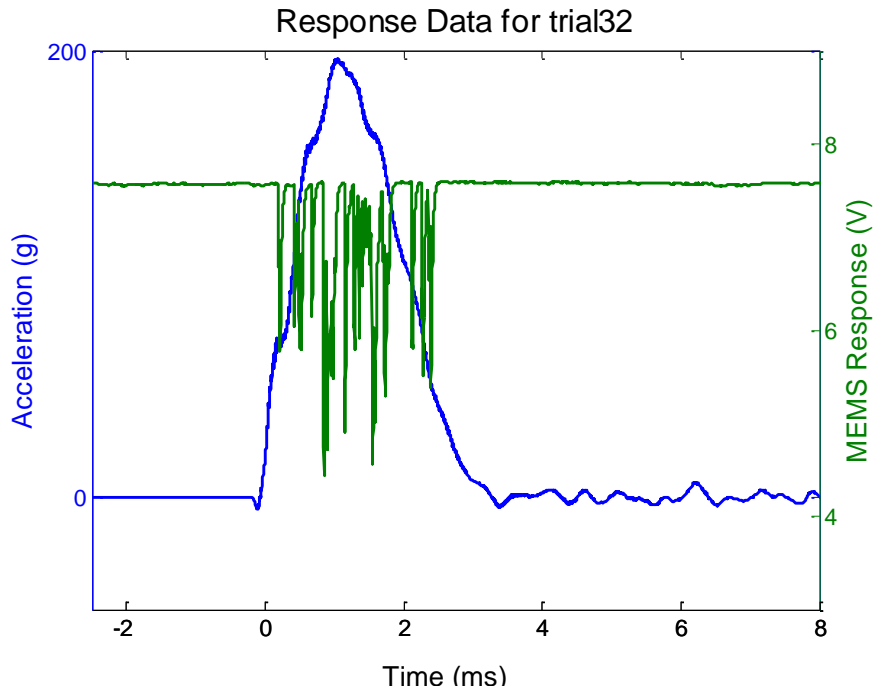


Figure 5: Successful measurement of a parallel combination of design type 2 (8- μm wide) cantilevers triggering at 67.27 g for a peak applied profile of 196.4 g

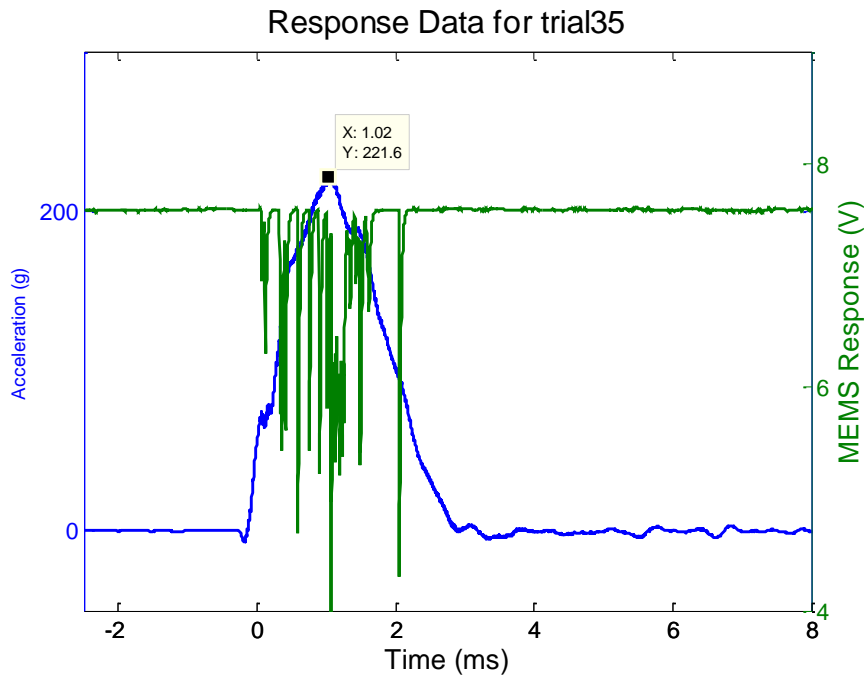


Figure 6: Successful measurement of a parallel combination of design type 2 (8- μm wide) cantilevers triggering at 70.86 g for a peak applied profile of 221.6 g

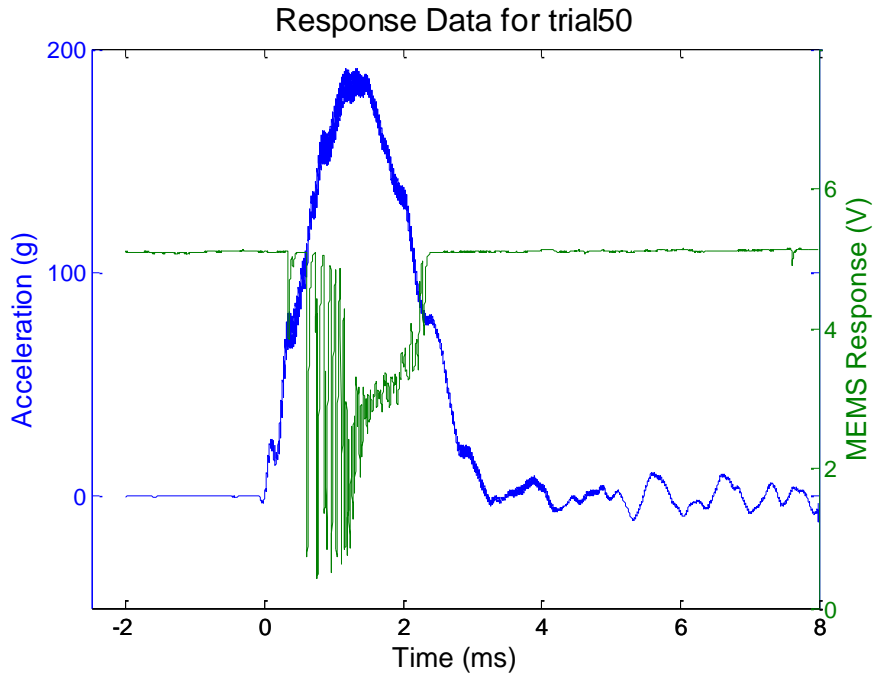


Figure 7: Successful measurement of a parallel combination of design type 2 (8- μm wide) cantilevers triggering at 79.14 g for a peak applied profile of 191 g

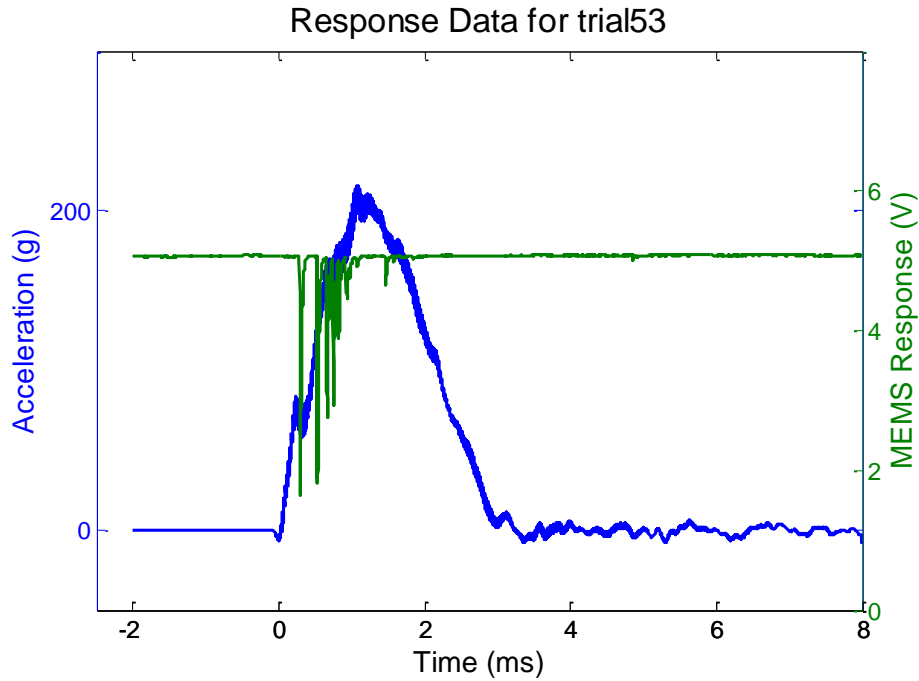


Figure 8: Successful measurement of a parallel combination of design type 2 (8- μm wide) cantilevers triggering at 77.6 g for a peak applied profile of 215.9 g

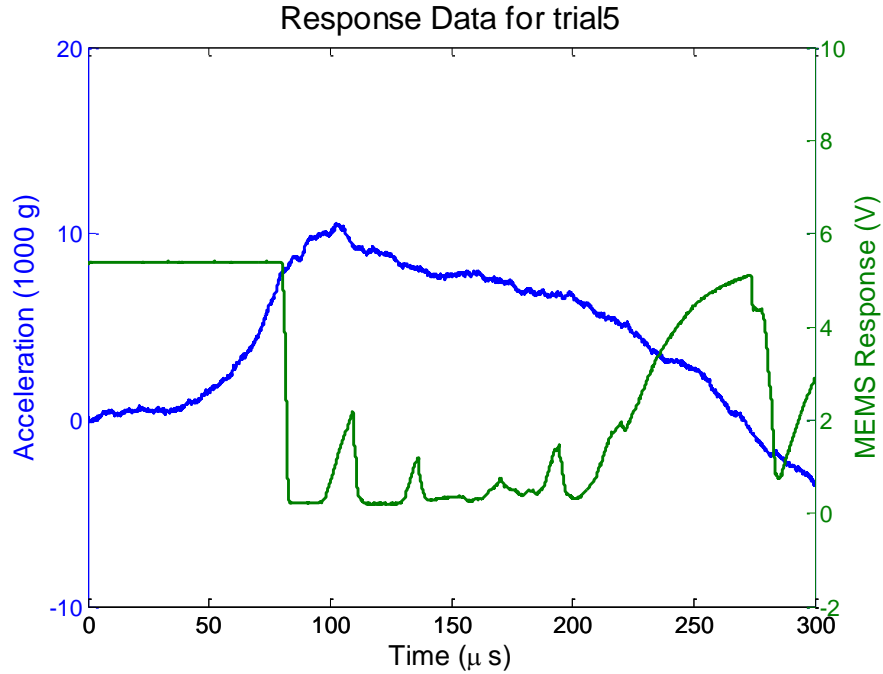


Figure 9: Successful measurement of a parallel combination of design type 2 (8- μm wide) cantilevers under an impact load of 10,380 g

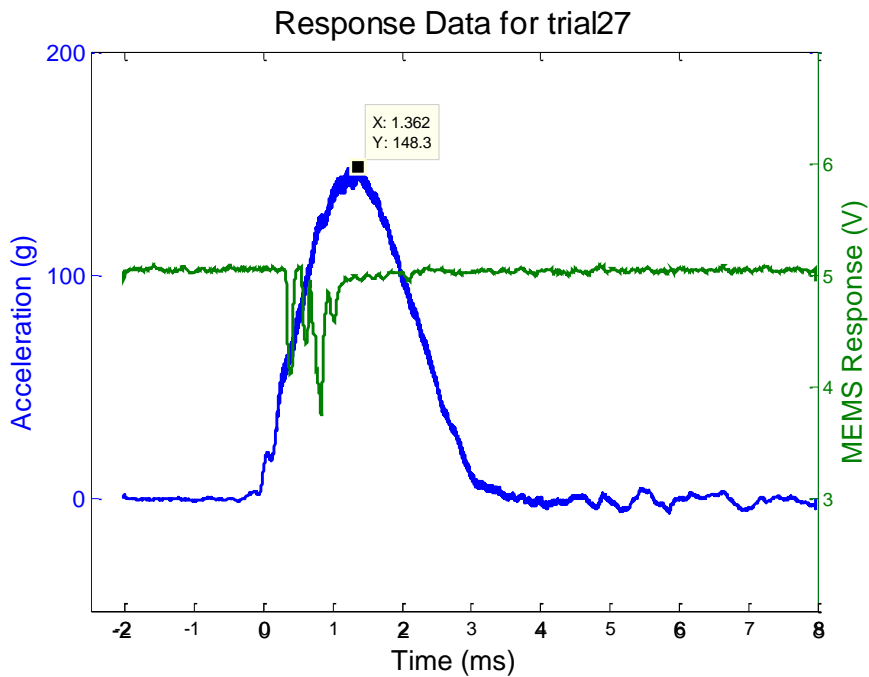


Figure 10: Successful measurement of a parallel combination of design type 2 (8- μm wide) cantilever after the above impact load of 10,380 g in Figure 7 triggering at 64.77 g under a applied load of 148.3 g

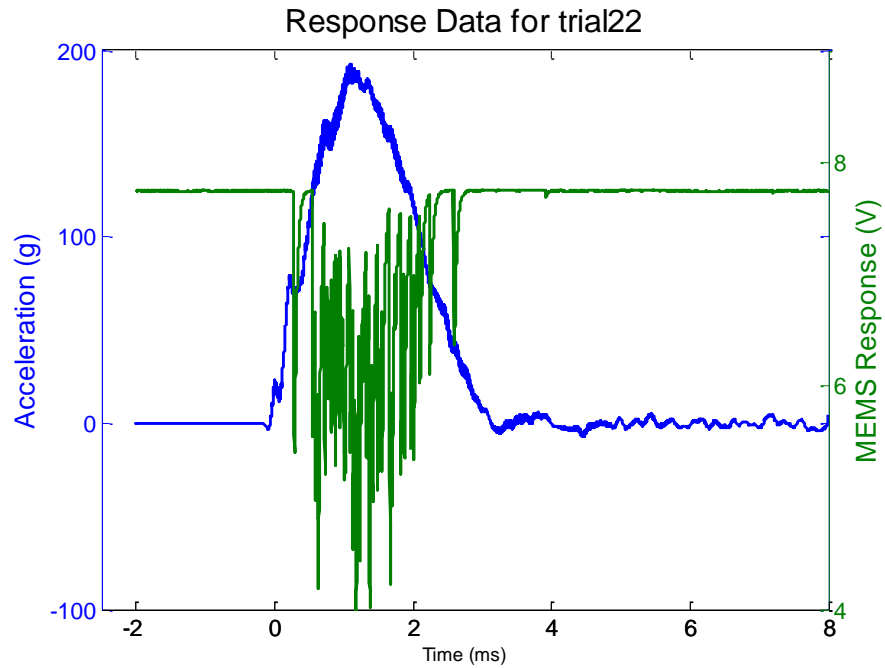


Figure 11: Successful measurement of a parallel combination of design type 2 (6- μm wide) cantilevers triggering at 69.07 g for a peak applied profile of 191.5 g

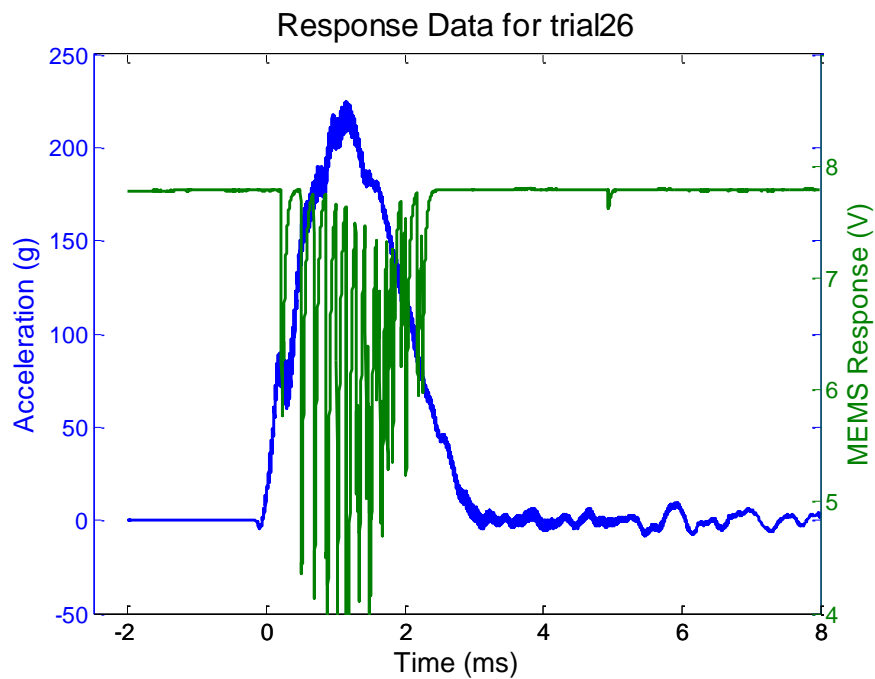
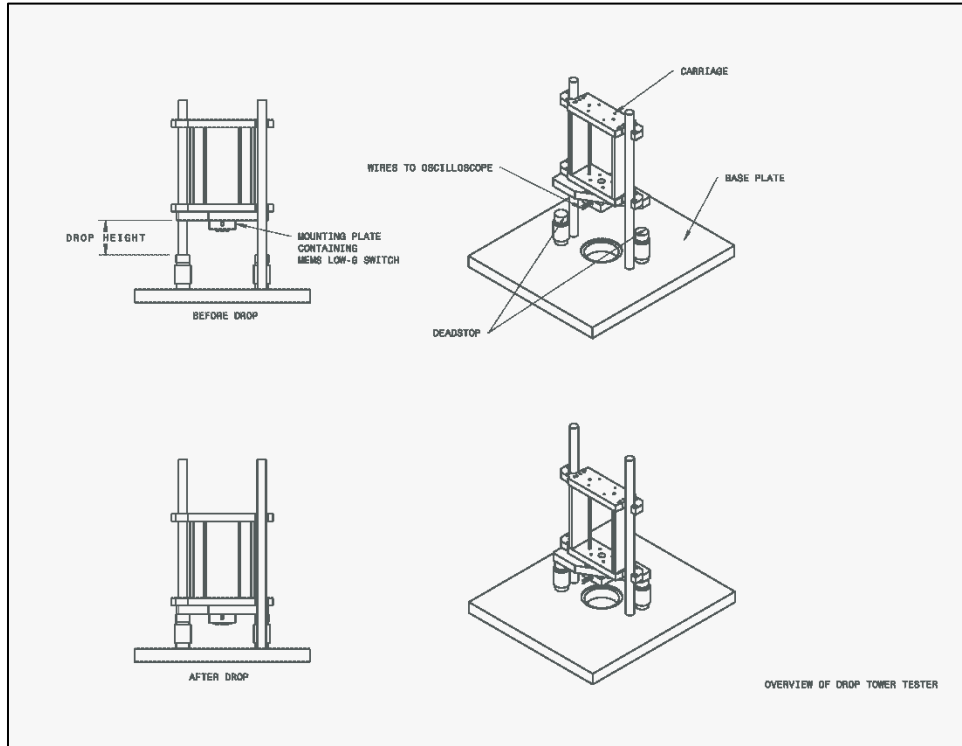
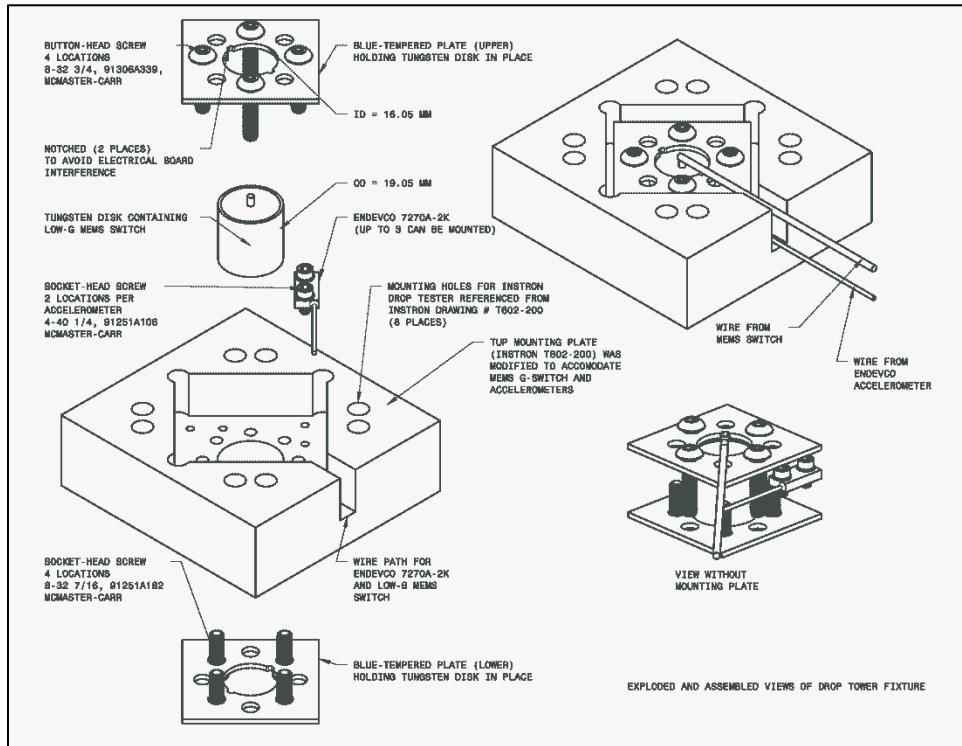


Figure 12: Successful measurement of a parallel combination of design type 2 (6- μm wide) cantilevers triggering at 73.58 g for a peak applied profile of 224.5 g

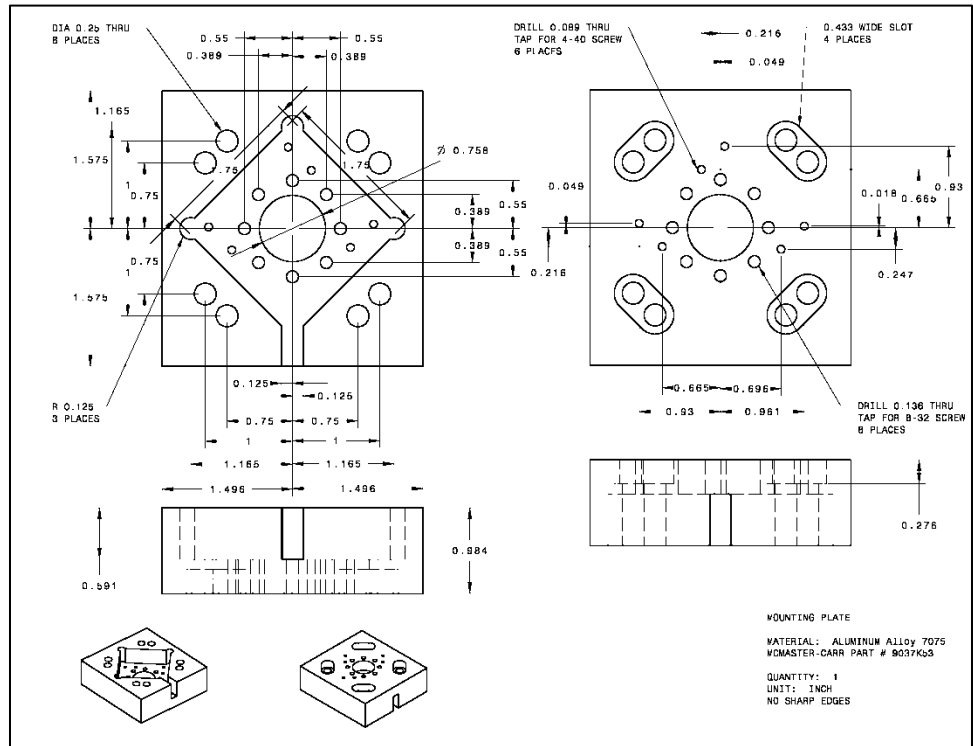
Appendix B



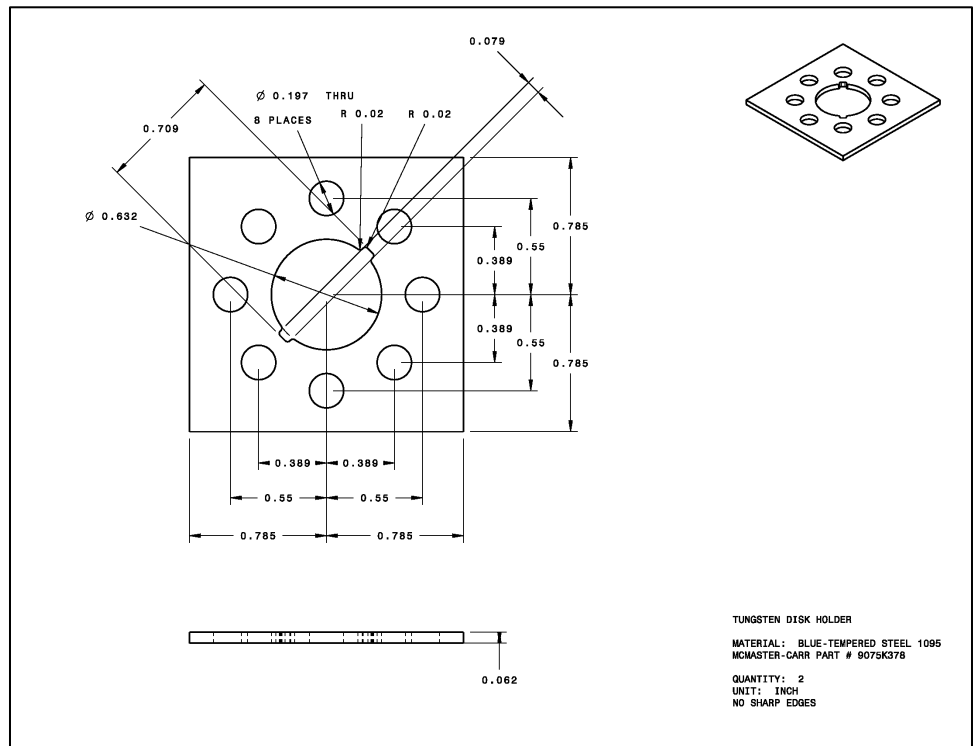
Drop tower fixture: Overview



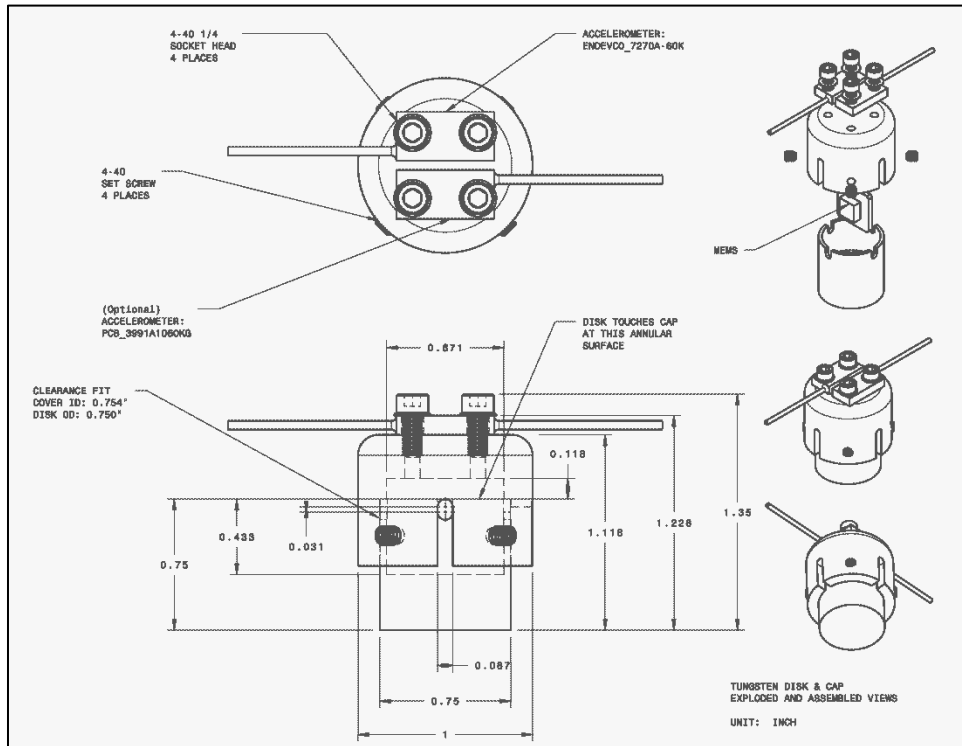
Drop tower fixture: Exploded and assembled view



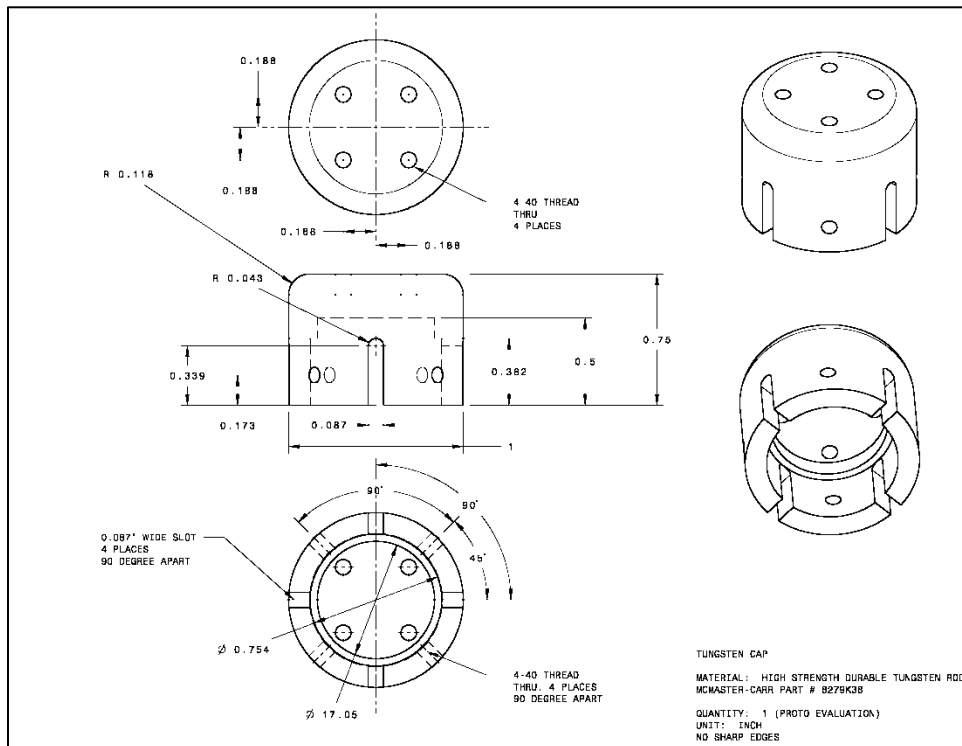
Drop tower fixture: Mounting plate



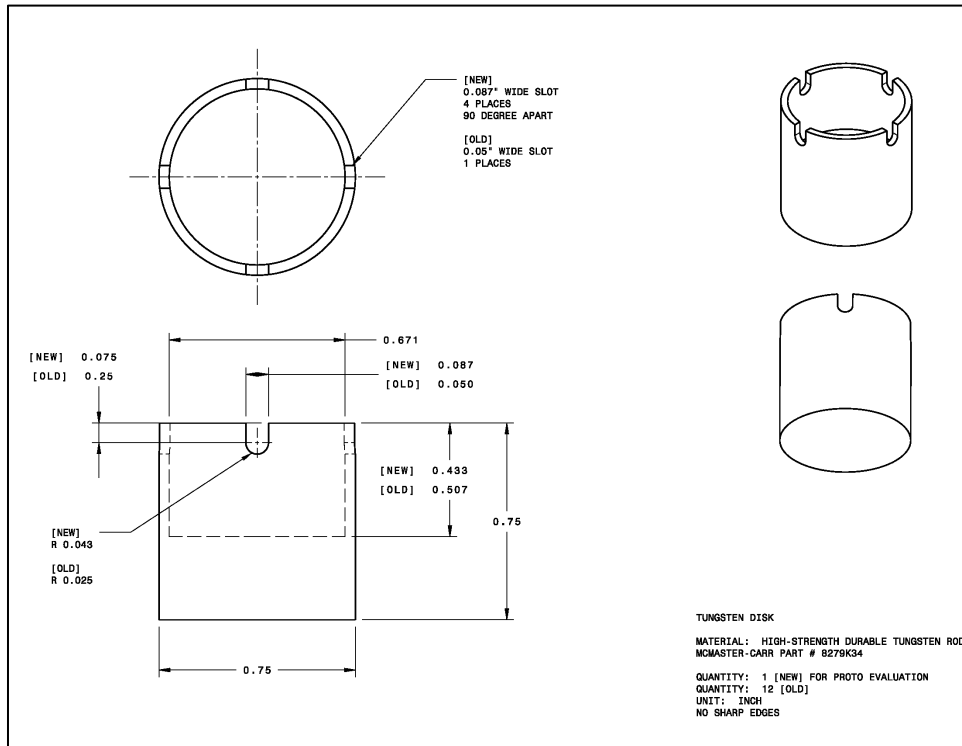
Drop tower fixture: Disk holder



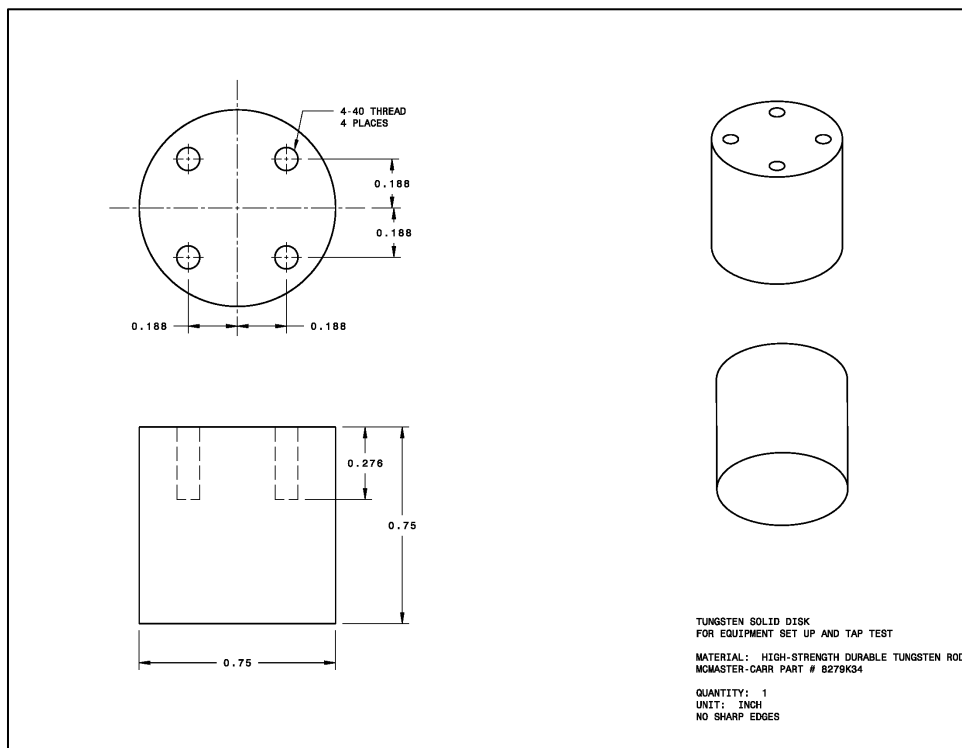
Kolsky bar fixture: Exploded and assembled view



Kolsky bar fixture: Tungsten cap



Kolsky bar fixture: Tungsten hollow disk



Kolsky bar fixture: Tungsten solid disk

DEPARTMENT OF DEFENSE

DEFENSE THREAT REDUCTION
AGENCY
8725 JOHN J. KINGMAN ROAD
STOP 6201
FORT BELVOIR ,VA 22060
ATTN: S. PEIRIS

DEFENSE TECHNICAL
INFORMATION CENTER
8725 JOHN J. KINGMAN ROAD,
SUITE 0944
FT. BELVOIR, VA 22060-6201
ATTN: DTIC/OCA

**DEPARTMENT OF DEFENSE
CONTRACTORS**

EXELIS, INC.
1680 TEXAS STREET, SE
KIRTLAND AFB, NM 87117-5669
ATTN: DTRIAC

PURDUE UNIVERSITY
3323 NEIL ARMSTRONG HALL OF
ENGINEERING
701 WEST STADIUM AVENUE
WEST LAFAYETTE, IN 47907
ATTN: W. CHEN